https://doi.org/10.5194/egusphere-2023-2504
Preprint. Discussion started: 8 November 2023

Multiscalar 3D characterisation of the Mid-Norwegian passive margin evolution, Central Norway: A multi-technique approach to unravelling the structural characteristics and tectonic history of offshore basement highs

Matthew S. Hodge[1]*, Guri Venvik[2], Jochen Knies[2], Roelant van der Lelij[2], Jasmin Schönenberger[2], Øystein Nordgulen[2], Marco Brønner[2], Aziz Nasuti[2], & Giulio Viola[1]

1: Department of Biological, Geological and Environmental Sciences, University of Bologna, Italy

2: Geological Survey of Norway (NGU), Trondheim, Norway

Correspondence to: Matthew S. Hodge (matthew.hodge@unibo.it)

Abstract. Smøla Island, situated within the Mid-Norwegian passive margin, contains crystalline basement-hosted intricate fracture and fault arrays formed during a polyphase brittle tectonic evolution. Understanding similar fracture patterns within basement structural highs offshore, which is crucial in that they are commonly associated with unconventional hydrocarbon reservoirs, remains challenging owing to the lack of rock exposure and geological and chronological constraints. As Smøla is an onshore analogue for basement highs offshore, any insights can therefore be applied to the offshore domain. In this study, we present a multiscalar multi-technique approach whereby various 2D and 3D field, drilling, geophysical, and K-Ar geochronology datasets are integrated to unravel the brittle evolution of Smøla and the surrounding margin. On the regional-scale, geophysical and DTM data-derived lineament analysis, along with local-scale field mapping, high resolution logging of four diamond drill holes, 3D modelling, and petrographic and microstructural analyses indicate that at least five deformation episodes affected Smøla through time. These deformation episodes are characterised by different geometric and kinematic patterns, and mineral assemblages: I) the earliest, ENE-WSW, WNW-ESE to NW-SE striking epidote-prehnite brittle structures are associated with syn to post-Devonian brittle sinistral transtension during post-Caledonian extension of the margin; II) NE-SW or NW-SE striking sericite-chlorite-calcite shear features formed from two separate brittle-ductile phases, which are related with both sinistral and later dextral strike-slip faulting during the Carboniferous to Late Triassic (~300 Ma to ~200 Ma); III) NE-SW, NNE-SSW striking chloritic-hematite breccias and gouges, linked to crustal extension, normal faulting, basin development (~200 Ma to ~100 Ma); IV) NE-SW to NNW-SSE and WNW-ESE striking hematite-zeolite-calcite veins and hydraulic breccias, likely associated to both late Mesozoic dextral strike-slip faulting, and regional ~E-W crustal extension (younger than ~150 Ma to ~75 Ma); and V) the last recorded episode characterised by NW-SE, WNW-ESE and NNE-SSW striking quartz-calcite veins cross-cutting all previous deformation features, associated with ~E-W to NE-SW crustal extension during the Cretaceous to Paleogene. Accordingly, 3D modelling of selected structures, by deformation

https://doi.org/10.5194/egusphere-2023-2504
Preprint. Discussion started: 8 November 2023

episode, reproduce the complex brittle arrays on Smøla through time. The structural modelling also highlights the multiscalar nature of basement deformation features, with modelled down-dip and strike extents of the structures varying by D_1-D_5. Overall, this 'toolbox' approach makes it possible to unravel the complex brittle deformation history of Smøla and the wider Mid-Norwegian margin and can be applied to other basement highs offshore Norway and elsewhere.

1 Introduction

Offshore crystalline basement highs are important structural elements of rifted passive margins (Peron-Pinvidic et al., 2013; Zastrozhnov et al., 2020). They are, however, very challenging to study when in deep oceanic waters and beneath younger sedimentary cover. Constraining their structural characteristics and tectonic evolution in those settings typically relies on relatively low-resolution datasets, such as seismic surveys and scattered drill hole data (e.g., Holdsworth et al., 2019; Tanner et al., 2020), which limits detailed reconstructions. Most of the geological knowledge on offshore basement highs derives from hydrocarbon exploration work, which, however, until recently only focussed on and around their outermost edges, with limited interest in the basement volumes themselves (Riber et al., 2015). On the other hand, following indications that fractured and weathered basement may represent productive unconventional hydrocarbon reservoirs or act as pathways for oil and gas migration, they have also recently begun to receive considerable attention (e.g., Hartz et al., 2013; Trice, 2014; Riber et al., 2015; Belaidi et al., 2018; Holdsworth et al., 2019).

In particular, in addition to reconstructing the details of their geological history, research has specifically focused on understanding basement-related permeability and fluid storage potential (e.g., Ceccato et al., 2021) as driven by the local pervasive fracture and fault systems (Stober & Bucher, 2007), together with rock weathering, seismic-resolution fracture patterns, bounding fault structures, and controls on the basement high geometries (e.g., Bonter & Trice, 2019; Faleide et al., 2008; Muñoz-Barrera et al., 2020; Rønning & Elvebakk, 2005; Skilbrei et al., 2002).

Crucially, a conceptual 'gap' remains relating to the understanding of the effective role of 'intrabasement' structures in an offshore context. These structures offshore are difficult to study because they are commonly sub-seismic resolution-scale in size (Tanner et al., 2020). Consequently, characterising geological structures that range in size from the sub-seismic resolution through to regional-scales, and resolving a related and potentially long-lived tectonic evolution, cannot be done from low resolution data alone. To mitigate these challenges, analogue onshore basement exposures are attracting researchers' attention as they provide significant advantages such as more extensive and ready site access, and data availability at regional to micro-scale resolutions.

Smøla Island, within the Mid-Norwegian passive margin, is a subaerial exposure of crystalline basement rocks (Fig. 1). The island is an ideal natural laboratory where to study an analogue of basement highs offshore Central Norway, owing to both its

https://doi.org/10.5194/egusphere-2023-2504
Preprint. Discussion started: 8 November 2023

proximity to the offshore Frøya High, and the similarity of basement geology found at both locations (Rønning and Elvebakk, 2005; Slagstad et al., 2011). As such, Smøla represents a wealthy archive of evidence of local and regional-scale structural features, which, if properly interpreted, may yield much information on the tectonic episodes that have affected the margin through time. Any geological insights from Smøla could then potentially be applied to basement highs offshore, thus aiding the reconstruction of their tectonic evolution and improving hydrocarbon exploration strategies.

The tectonic evolution of onshore basement exposures along the Norwegian passive margin has been worked on by, amongst others, Redfield et al. (2004), Davids et al. (2013), Viola et al. (2016), Ksienzyk et al. (2016), Scheiber et al. (2016), Scheiber and Viola (2018), and Fossen et al. (2021), with the most recent insights over the Mid-Norwegian portion by Tartaglia et al. (2022). Although previous studies provide tight constraints, applying a novel multi-technique and multiscalar approach to unravelling complex deformation patterns on an onshore basement exposure may provide important new insights to this existing work.

Here we describe and test a comprehensive workflow for characterising onshore basement blocks. The adopted tools include surface geological- (outcrop mapping and sampling), structural and petrographical, in addition to regional datasets (airborne magnetic surveys and digital terrain models - DTMs). This approach is further augmented by an unprecedented 3D perspective afforded by four oriented diamond drill holes. They provide fresh basement exposures and insights into complex structures down to the centimetric scale.

Aided by this multiscalar 3D approach we expand on the existing tectonic evolution models for the Mid-Norwegian passive margin. We describe and classify the variety of basement-hosted multiscalar deformation features present in regional aeromagnetic imagery, DTM's, drill core, field outcrops, and thin sections. This approach is further strengthened by applying K-Ar geochronology, which constrains the absolute time dimension of the reconstructed tectonic phases. Finally, as fault and fracture arrays in crystalline basement rocks control the local secondary permeability (Gillespie et al., 2020), our work has implications on understanding offshore basement high-hosted unconventional hydrocarbon reservoirs, and basement deformation more generally, providing crucial deterministic inputs to future studies aiming to model basement fracturing and petrophysical behaviour.

2 Geological framework

2.1 Regional perspective

Smøla Island, located in Central Norway, is set within the Mid-Norwegian passive margin, (Figure 1A), a region shaped by a prolonged and complex geological history (Peron-Pinvidic & Osmundsen, 2020). The island (Figure 1B) is comprised by 445.7 ± 3.8 Ma plutonic magmatic-arc rocks (Tucker et al., 2004; Slagstad et al., 2011) and oceanic crustal units, all of which were

https://doi.org/10.5194/egusphere-2023-2504
Preprint. Discussion started: 8 November 2023

emplaced and accreted just prior to the Silurian-Devonian (~430 Ma) Scandian Phase of the Caledonian Orogeny (Corfu et al., 2014; Gee et al., 2008; Slagstad & Kirkland, 2018; Tucker et al., 2004). Caledonian shortening led to nappe and thrust fault development, with transposition of the Smøla rocks along major detachments over both the allochthonous continental Neoproterozoic Baltoscandian nappes and the underlying autochthonous Palaeo- to Mesoproterozoic Baltican crystalline basement of the Western Gneiss Region (WGR) (Fossen, 1992; Tucker et al., 2004; Corfu et al., 2014) (Figure 1C).

During the Early Devonian (Late Caledonian times), orogenic collapse of the by then overthickened orogen resulted in significant crustal extension by both reactivation of favourably oriented contractional structures (Fossen, 2010; Fossen et al., 2017) and development of new crustal-scale extensional shear zones and exhumation (Figure 1) (Osmundsen et al., 2006). Late Caledonian extension also caused the Smøla rocks to be translated, with both strike-slip offset and down-faulting across the Møre-Trøndelag Fault Complex (MTFC), a regional fault system with multiple strands and complex kinematics that was repeatedly activated through time (Redfield et al., 2004; Watts et al., 2023). Smøla experienced limited metamorphic overprint (on average sub-greenschist facies conditions) and only localised ductile deformation (Tucker et al., 2004). Also associated with the Devonian tectonic inversion, extensional (possible pull-apart) basins formed in response to brittle extensional faulting, such as the MTFC-related Edøyfjorden Basin proximal to Smøla (Bøe et al., 1989; Bøe & Bjerkli, 1989; Fossen et al., 2017; Osmundsen et al., 2006).

Post-Caledonian extension and rifting continued to the Late Cretaceous/Early Palaeocene, eventually leading to the break-up of Greenland from the Eurasia plate at ~54 Ma and opening of the North Atlantic (Peron-Pinvidic and Osmundsen, 2018; Bunkholt et al., 2022).

During this time, the Mid-Norwegian passive margin first formed and then underwent several tectonic phases which include rift initiation during the Carboniferous, crustal stretching and rifting during the Permo-Triassic, Late-Triassic to Jurassic crustal thinning, renewed Mid-Jurassic to Early Cretaceous rifting with hyper-extension of the margin during the Late-Cretaceous to Paleocene, and early seafloor formation and spreading during the Paleocene-Eocene (Mosar et al., 2002; Faleide et al., 2008; Peron-Pinvidic and Osmundsen, 2018).

https://doi.org/10.5194/egusphere-2023-2504
Preprint. Discussion started: 8 November 2023

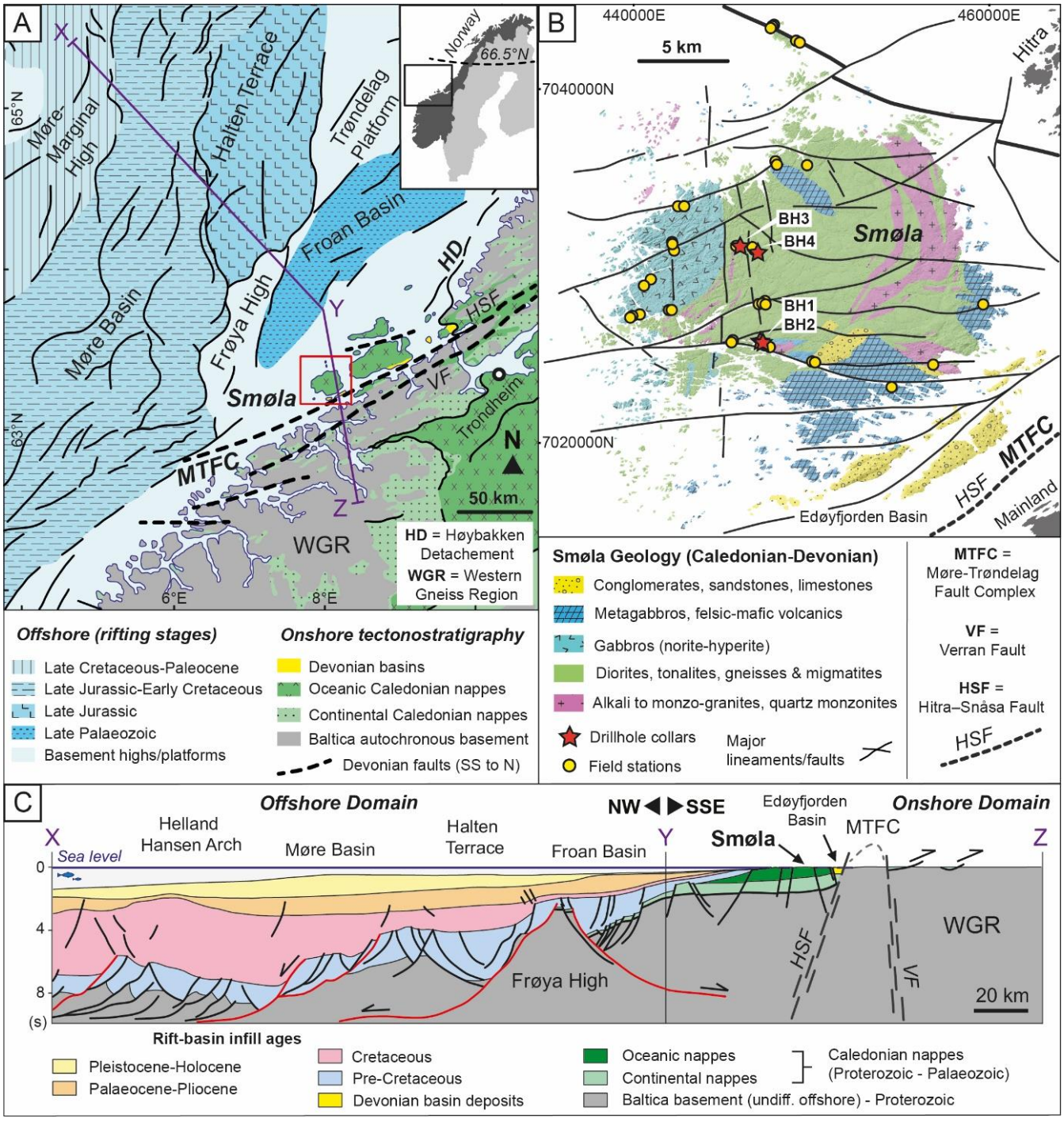

Figure 1. Summary figure detailing the geological context of Smøla Island, Central Norway. A) Regional setting of Smøla on the Mid-Norwegian Passive margin. Smøla is separated from the Western Gneiss Region (WGR) by the Møre-Trøndelag Fault Complex (MTFC), with two fault strands, the Hitra–Snåsa Fault (HSF) and the Verran Fault (VF). The Høybakken Detachement (HD) is shown to the NE of Smøla. To the NW of Smøla, in the offshore domain, major basins are present (e.g., Møre Basin), bound by normal faults and structural highs (e.g., Frøya High) (modified from Faleide et al., 2008; Bedrock map of Norway, Geological Survey

https://doi.org/10.5194/egusphere-2023-2504
Preprint. Discussion started: 8 November 2023

of Norway, 2021)**. B) The local geology of Smøla Island, showing the Caledonian and Devonian geology. Significant lineaments and faults (interpreted from airborne geophysics, DTM, and field studies) crosscut the island. The trace of the MTFC (HSF strand) is indicated. The drill holes (red stars) and outcrop mapping locations (yellow circles) are shown** (modified from Fediuk and Siedlecki, 1977)**. C) Onshore-offshore interpretive geological cross section (X-Y-Z) as shown in Panel A, showing major regional structures and crustal anatomy relative to Smøla. Including the two strands of the MTFC (HSF and VF) and the Frøya High offshore** (modified from Zastrozhnov et al., 2020)**.**

These events produced discrete generations of basins (such as the Froan, Vøring, and Møre Basins) along the newly-forming Norwegian shelf, which progressively infilled with synrift sediments (Figure 1A & C) (Faleide et al., 2008; Zastrozhnov et al., 2020). In places, structural highs of Caledonian-aged and underlying Baltica crystalline basement, such as the Frøya High to the NW of Smøla formed through rift-related exhumation between these basins (Muñoz-Barrera et al., 2020) leading to remarkable host and graben series. Bounding the structural highs and the different basins, are crustal-scale extensional faults (Figure 1A & C) (Mosar et al., 2002; Skilbrei et al., 2002). Overall, this protracted rifting and hyper-extension history resulted in a highly attenuated offshore domain, reactivating, and overprinting the existing Caledonian deformation features (Figure 1A & C) (Mosar et al., 2002; Zastrozhnov et al., 2020).

2.2 The geology of Smøla

Smøla is composed of several Caledonian-aged bedrock types traditionally attributed to the Caledonian Upper Allochthon (Roberts & Gee, 1985) (Figure 1B), including diorite (the most common lithology), gabbro, tonalite, alkali granite, quartz monzonite to monzo-granite, quartz-feldspar and amphibolite-biotite gneiss, limestone and volcanic rocks (andesitic to rhyolitic in composition in a faulted block on the SE-portion of Smøla). Late, felsic to mafic dykes crosscut all other rock types (Brunton & Bockelie, 1979; Fediuk & Siedlecki, 1977; H. Gautneb, 1988; Ha. Gautneb & Roberts, 1989; Roberts, 1980). In addition to the 445.7 ± 3.8 Ma (1σ) U/Pb intrusive age of a dated granodiorite (Tucker et al., 2004), a granitic dyke was dated to 428 ± 10 Ma (2σ) (Rb/Sr) (H. Gautneb, 1988), providing an Ordovician-Silurian age envelope for the plutonic rocks on the island. To the S and SE of Smøla (e.g., Edøyfjorden Basin – Figure 1B) the Caledonian bedrock is unconformably overlain by the late Silurian-mid Devonian sedimentary cover of the Smøla Group, and later Jurassic-Cretaceous sedimentary successions (Bøe et al., 1989; Bøe & Bjerkli, 1989; Fediuk & Siedlecki, 1977). These include siliciclastic deposits of red-oxidised polymictic conglomerate, siltstone, and sandstone (Bøe et al., 1989), and infill Devonian extensional basins along the MTFC (Bøe & Bjerkli, 1989).

Continuing to the S and SE of Smøla (and bounding the Devonian basin), the NE-SW striking MTFC is the most proximal and dominant regional-scale structural feature to the island. This wide (10 to 50 km) structure extends for >600 km from Central Trøndelag into the northern-part of the North Sea, and branches into two sub-parallel strands, the Hitra–Snåsa Fault (HSF) to the NW (the most proximal to Smøla), and the Verran Fault (VF) to the SE (Figure 1A, B, & C) (Olsen et al., 2007; Watts, 2001; Watts et al., 2023). The kinematic evolution of the MTFC is complex, with a polyphase deformation history from the Devonian until the Cenozoic (e.g., Grønlie and Roberts, 1989; Seranne, 1992; Watts, 2001; Redfield et al., 2004; Tartaglia et

https://doi.org/10.5194/egusphere-2023-2504
Preprint. Discussion started: 8 November 2023

al., 2022; Watts et al., 2023). In comparison to the MTFC and the wider margin, the post-Caledonian structural evolution of Smøla remains poorly investigated and understood.

3 The applied toolbox

This study's multi-technique approach involves a variety of 2D and 3D datasets, ranging from the regional-scale through to the micro-scale. Integrated into this array of datasets is also the absolute time dimension, provided through K-Ar geochronology of structurally well-characterised fault rocks, which provides chronological constraints on all other datasets. We briefly outline below the applied toolbox, with a more detailed description in the supplementary material.

3.1 Geophysical and remote sensing data and lineament mapping

The geophysical data used in this study was acquired by the Geological Survey of Norway (NGU) (Nasuti et al., 2015), with details on survey parameters and data processing available in the supplementary material. Our lineament picking and mapping followed White (2014) and Scheiber and Viola (2018), making use of both the magnetic geophysical and DTM imagery within a geographic information systems (GIS) software platform (Figure 2). The description of the methodology used to identify and place the lineaments is also available in the supplementary document.

3.2 Drill hole logging and field methods

Geological features in the drill cores (Figure 3) were systematically logged downhole (for a total investigated length of 364.9 m) of diamond drill core, recording lithology and rock alteration, deformation types, fracture/fault characteristics, mineral infill, and cross-cutting relationships. The methodology used to measure structural data in drill core followed both the methods of Holcombe (2013) and Blenkinsop et al. (2015). A more detailed description of the methodology is available in the supplementary material. The field-based structural data acquisition involved typical field methods, which initially aimed at ground-truthing possible exposed deformation zones identified in the lineament mapping, and the systematic mapping of representative outcrops (Figure 1B). In total sixty-six outcrop sites were studied, with data collected recording deformation feature types, fracture/vein mineral infill, fault slip information, host rock lithology, and cross-cutting/genetic relationships between the various features.

3.3 X-ray diffraction and K-Ar dating

Seven structurally-controlled fault gouge and breccia samples were collected (Figure 8) from fault and deformation zones in both drill core and outcrop, and subsequently processed at the dedicated NGU laboratory in Trondheim, Norway. Initially, all the samples were disintegrated and separated into <0.1 µm, 0.1-0.4 µm, 0.4-2 µm, 2-6 µm, 6-10 µm size fractions. Each of these size fractions then underwent quantitative analysis for both potassium (K) and argon (Ar) using total digest ICP-OES, and a Isotopx NGX multi collector noble gas mass spectrometer system respectfully. X-ray diffraction (XRD) analysis was

https://doi.org/10.5194/egusphere-2023-2504
Preprint. Discussion started: 8 November 2023

performed on each fraction to determine and quantify the mineralogical composition. A full description of both XRD and the K-Ar analysis methodology is available in the supplementary material and in Viola et al. (2018).

4 Results

4.1 Lineament mapping from geophysics and DTM data

The analysis of regional-scale features such as geophysical lineaments and topographic features (Figure 2) formed the initial stage of the study. These features occur on the kilometre-scale and can be traced over large areas both off- and onshore.

The >2000 mapped lineaments are linear to curvilinear and at times irregular features and crosscut or separate the different magnetic blocks discussed above. The lineaments are classified based on length and hierarchy of formation: 1st order lineaments are potentially major regional structures, while 2nd order lineaments are commonly major splays or secondary structures off the 1st order lineaments, or form domain boundaries between magnetic blocks, and are commonly >10 km in length; 3rd order lineaments are all the other lineaments, which are typically <10 km in length.

Together, the 1st, 2nd, and 3rd order lineaments possess at least eight dominant orientation trends over the study area, with various age and cross-cutting relationships between the different lineament trends. These age relationships and the spatial distribution of the specific lineament trends by domain area are summarised in Table 1, and selectively illustrated in Figure 2B.

https://doi.org/10.5194/egusphere-2023-2504
Preprint. Discussion started: 8 November 2023

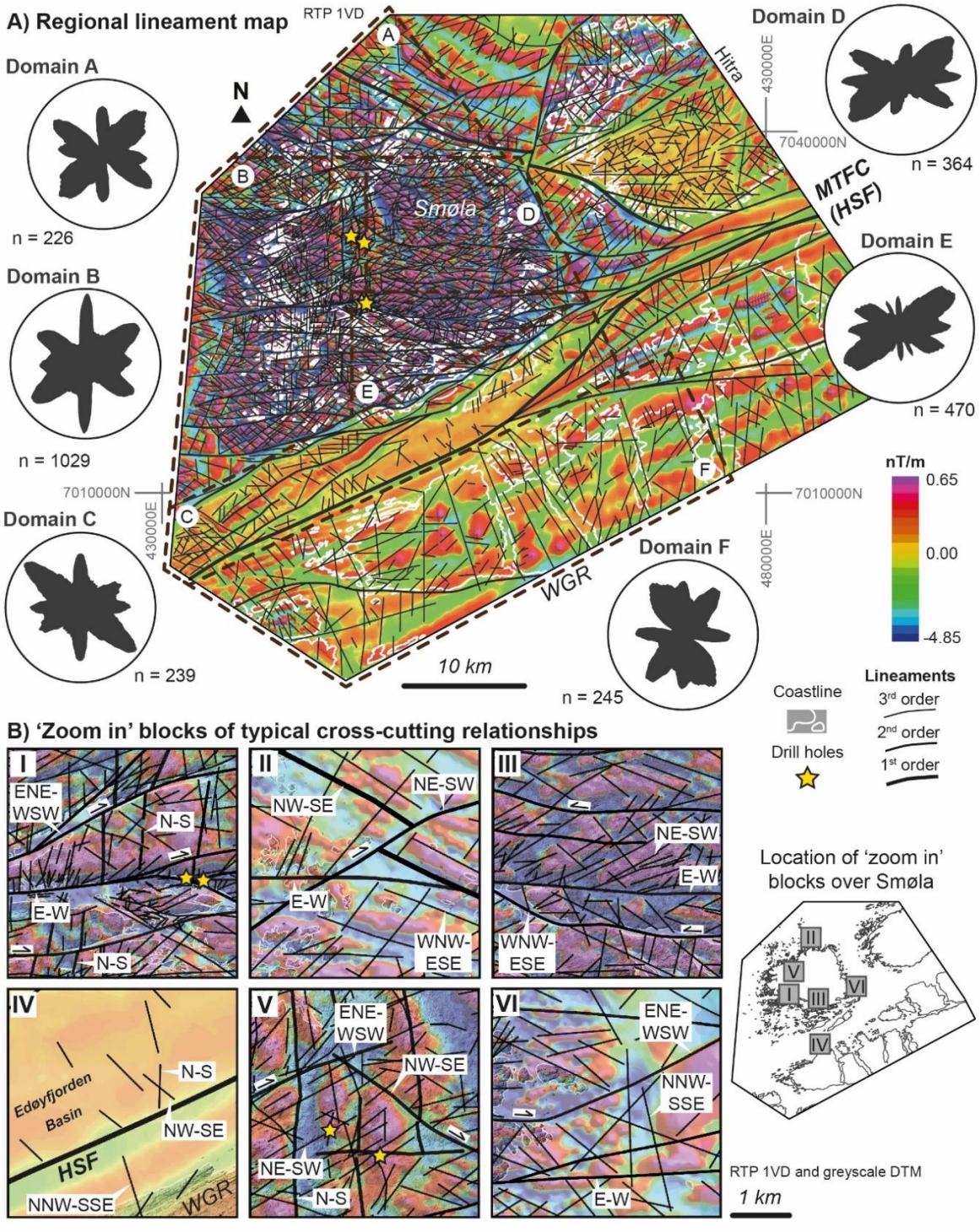

Figure 2. A) Airborne magnetic survey imagery (reduced to pole – first vertical derivative (RTP-1VD)) over Smøla Island and surrounding areas (coastline shown in white). Displayed over the magnetic imagery are 1st, 2nd, and 3rd order lineaments mapped

https://doi.org/10.5194/egusphere-2023-2504
Preprint. Discussion started: 8 November 2023

from both the magnetic data and DTM data. Airborne magnetic survey imagery from Nasuti et al. (2015). The area over Smøla onto the WGR region is domained A (north of Smøla), B (western and SW of Smøla), C (area over the MTFC), D (NE Smøla), E (SE Smøla), and F (WGR area). Rose plots of strike trends of mapped lineaments are shown by domain. B) 'Zoom in' blocks showing representative examples of cross-cutting relationships between the different lineament trends. Locations of the 'zoom in' blocks are displayed on the adjacent schematic map of Smøla.

Table 1. Age relationship matrix between the main lineament trends, with the occurrence and relative abundance (letter order) in the domain areas of Figure 2. Relationship types include m = mutual cross-cutting, x(s) = cross-cutting with sinistral offset, x(d) = cross-cutting with dextral offset, x(i) cross-cutting with dip-slip offset, x(r)=cross-cutting with reactivation of older lineament, a = abutting/terminating.

		Younger								
	Lineaments	N-S	NW-SE	E-W	ENE-WSW	NE-SW	WNW-ESE	NNE-SSW	NNW-SSE	Domain
Older	N-S		m, x(d)	x(d, s, i?)	x(d, s, i?)	x(d)	x(s)	x	x, a	B, A, C, F
	NW-SE	m		x(d)	x(d, s)	x(d)	x(s)	x	m, a	B, D, E, A, C
	E-W		x(r)		m	a	m	a,x	x, a	E, D, C, A
	ENE-WSW			m		a	x(s)	x?	x	C, B
	NE-SW		a, x(d, r)				a	x, a	x(i?), a	A, D, E, B, F
	WNW-ESE			m		a		a	x?	A, F
	NNE-SSW			m, x(r)	x(r)				m?	D, B
	NNW-SSE		m					m?		F, E

The N-S lineaments, typically 3rd to 2nd order lineaments, are cross-cut by all other lineaments, except for the NNW-SSE lineaments which, in places, abut against the N-S lineaments (Figure 2B.I). The N-S and NW-SE lineaments are likely coeval or conjugate owing to their local mutual cross-cutting relationships. The N-S and E-W, ENE-WSW lineaments have complex cross-cutting relationships (Figure 2B.I and B.V), with the N-S lineaments being dextrally, sinistrally, and possibly dip-slip offset (possible multiple reactivations) in places. The N-S lineaments are most common in the western-part of Smøla and offshore, within Domains B and A. The NW-SE lineaments are similarly offset by many of the other lineaments (Figure 2B.II), although the E-W lineaments only dextrally offset the NW-SE lineaments (Figure 2B.III), and there is no apparent dip-slip offset by any other lineaments. The NW-SE lineaments offset the E-W and the NE-SW lineaments, as well as the magnetic grain (Figure 2B.V), but this may be due to later reactivations (typically dextral offsets). The NW-SE and the NNW-SSE lineaments have rare mutual cross-cutting relationships (Figure 2B.VI), but otherwise the NNW-SSE tend to terminate up against the NW-SE lineaments. The NW-SE lineaments are most common over domains B, D, E, and in the north in Domain A.

The E-W lineaments, frequently classed as 2nd order lineaments and representing possible fault splays or Riedel shears off the 1st order lineament representing the HSF (Figure 2A), are cross-cut by NW-SE, NNE-SSW and NNW-SSE lineaments (Figure 2B.II, B.III). The E-W lineaments also exhibit mutual cross-cutting (potentially coeval) relationships with ENE-WSW (which

https://doi.org/10.5194/egusphere-2023-2504
Preprint. Discussion started: 8 November 2023

are splays of the E-W structures) and WNW-ESE (Figure 2B.I, B.III) lineaments. All three lineament trends possess similar cross-cutting relationships with the other lineaments, although the WNW-ESE lineaments only sinistrally offset both the N-S and NW-SE lineaments, with no local dextral offset. The NE-SW lineaments are clustered on and abut against the N/NE sides of the E-W lineaments and the WNW-ESE rotations (Figure 2B.I, B.III), possibly representing 3rd order Riedel shears or splays off the 2nd order E-W lineaments. The E-W lineaments are most common in the central portion of Smøla, in Domains E, D, C (on the NW side), and A.

The NE-SW lineaments are typically 3rd order lineaments (Figure 2B.V). They form prominent elongate topographical valleys in the DTM of western Smøla. These lineaments dextrally offset both the N-S and NW-SE lineaments (including a 1st order lineament), and abut against the E-W, ENE-WSW, and WNW-ESE lineaments (as mentioned above). The NE-SW lineaments are, however, locally offset by possibly reactivated NW-SE, NNE-SSW, and NNW-SSE lineaments (with a possible dip-slip component), although these other lineaments frequently terminate against the NE-SW lineaments. Overall, the NE-SW lineaments are pervasive across Domains A, D, E, B, and F, but are nearly absent in Domain C.

The two least common lineament trends, the NNE-SSW and NNW-SSE lineaments, mutually crosscut one another, although this is mostly seen in the Domain F (Figure 2A). Similarly, apparent late reactivated NW-SE lineaments display similar mutual cross-cutting relationships. Overall, these lineaments either crosscut or abut against all other lineaments without being crosscut and offset by any other lineament (Figure 2B.VI). They are most abundant in Domain D and B for the NNE-SSW lineaments, and Domain F and E for the NNW-SSE lineaments.

4.2 Deformation history

The availability of four diamond drill holes (Figure 1B and Figure 3) confers a novel 3D view into the geology of Smøla and this portion of the Mid-Norwegian passive margin. As the ~365 m of drill core is oriented, centimetric-scale logging provided an unprecedented high-resolution structural dataset, which, together with extensive direct field observations (Figure 1b), represents the foundation of this study. The drill holes intersect several deformation zones and a large array of deformation features, which are displayed downhole on Figure 3. An assortment of minerals has been systematically documented as decorating fracture surfaces, mineralising faults rocks, and infilling veins (Figures 4 and 5). The different mineral infill types and associated deformation features exhibit either coeval or crosscutting relationships, and orientation trends (Figure 6). As such, assemblages of coeval infill minerals have been used to group the documented deformation features and mineralisation based on the relative timing (summarised in Figure 7). The coeval mineral assemblages, also corresponding to consistent deformation styles and orientation trends, may represent distinct mineralisation events associated with discrete deformation episodes (e.g., Drake et al., 2009; Viola et al., 2009). We now systematically describe the progressive mineralisation and deformation history of the study area starting from the apparent earliest to the latest features as informed by the relative age

https://doi.org/10.5194/egusphere-2023-2504
Preprint. Discussion started: 8 November 2023

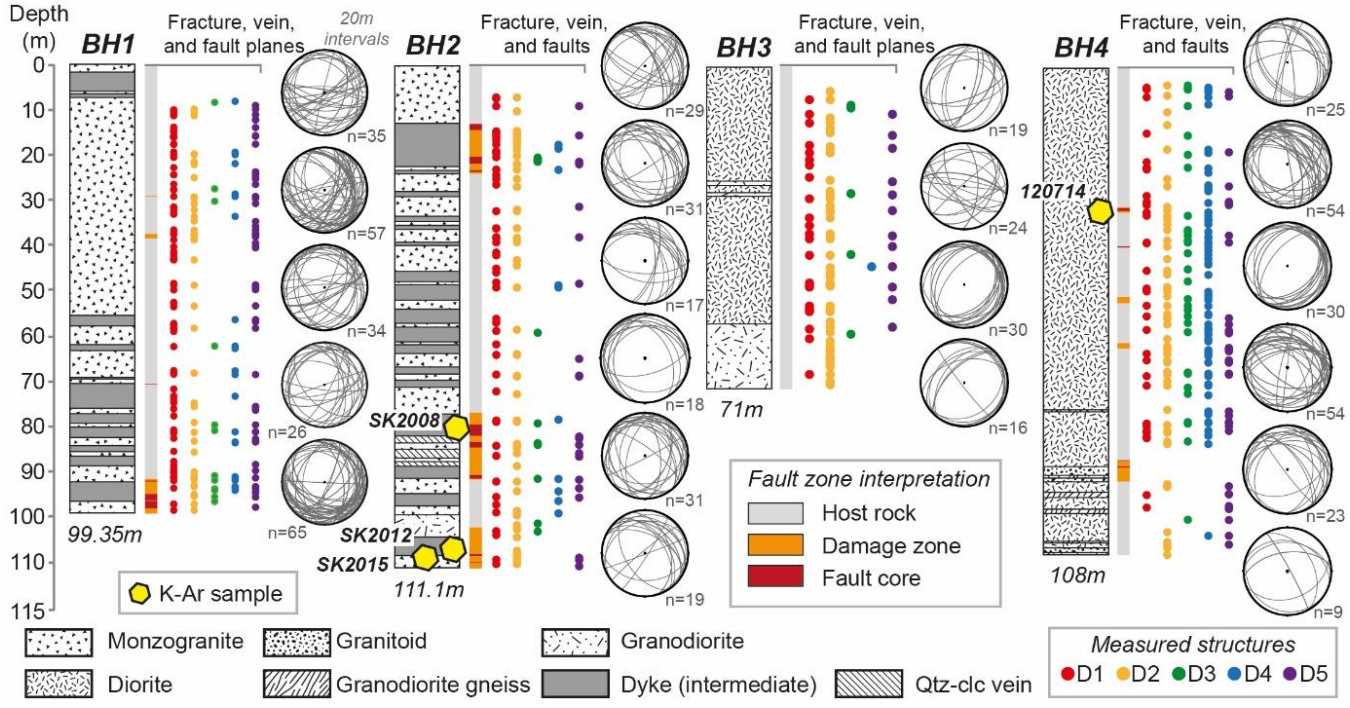

Figure 3. Graphic logs showing both downhole lithology and fault zone interpretations for each of the four Smøla diamond drill holes. Measured structural data is shown distributed downhole, grouped by mineral assemblage (and deformation episode), with D1 = epidote-prehnite, D2 = sericite-chlorite-calcite, D3 = chlorite-hematite (+/- calcite), D4 = hematite-zeolite-calcite, and D5 = quartz-calcite. Measured structures are also represented plotted as planes on the adjacent equal area stereonets. Each stereonet represents at least 20m of drill core and correspond to the downhole depths of the drill holes.

4.2.1 D_1: epidote-prehnite-stable faulting and veining

The earliest recognised brittle deformation features on Smøla are epidote and prehnite veins, hydraulic breccias, and cataclasites involving at least three different generations of epidote (epi 1, 2, and 3 on Figure 4A & B). These features are most commonly ENE-WSW striking, with other subordinate trends oriented WNW-ESE to NW-SE (Figure 6) and dip mostly steeply (~75°). They are strike- or oblique-slip features (commonly as top-to-the NNW normal-oblique faults).

The epidote mineralisation is either an early pale/light green-yellow (epi 1 and 2) or a later grass-green type (epi 3). The earlier epidote typically infills tensile or shear veins, with well-developed slickenside surfaces on the vein-host rock interfaces or internally on crack-seal surfaces (Figure 4A). The later grass-green epidote mineralisation, however, is different, occurring as infill of irregular, bifurcating to anatomising veins (Figure 4B), which in places crosscut and rework the early epidote. All three types cross-cut host rock lithological features, such as aplitic veins.

https://doi.org/10.5194/egusphere-2023-2504
Preprint. Discussion started: 8 November 2023

290

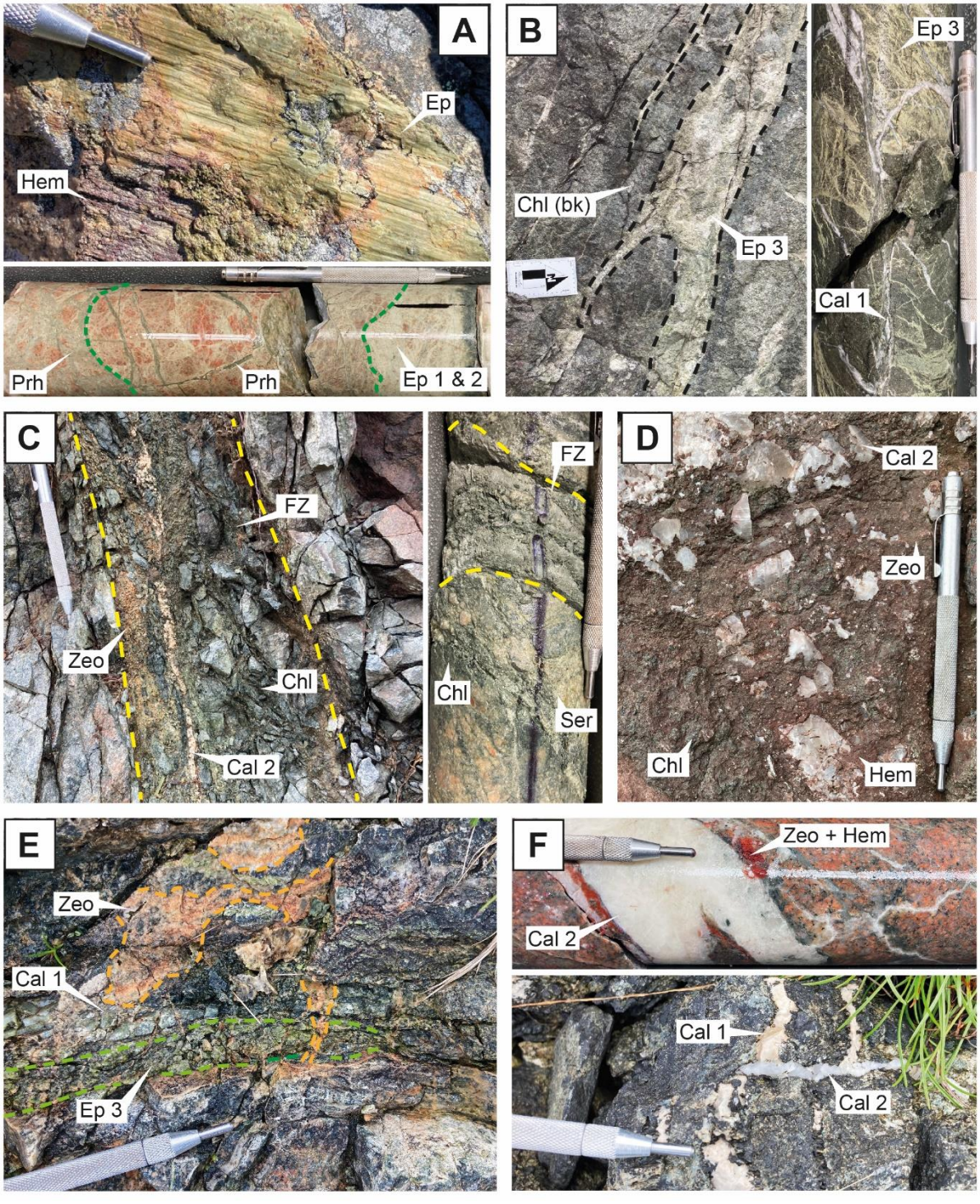

https://doi.org/10.5194/egusphere-2023-2504
Preprint. Discussion started: 8 November 2023

Figure 4. Representative examples of mesoscale deformation features on Smøla. A) Epidote slickenside surface (combination of light green and grass-green epidote) and light green epidote (Ep 1 and 2) veins and cataclasite being cross-cut by prehnite (Prh) vein breccia in BH1. B) Bifurcating diffuse veins of grass-green epidote (epi 3) with black chlorite (Chl (bk)); core-hosted abundant grass-green epidote veins are cross-cut by early calcite veins (Cal 1). C) Chloritic (Chl) fault zone (+/- sericitic) with later zeolite (Zeo) and calcite vein (Cal 2). The zone is highly fractured, the friable gouge (left side of the zone) represents a fault core; a similar narrow fault zone in BH2, with strong foliation and abundant sericite (Ser) infill. D) Chlorite (Chl)-hematite (hem) cataclasite veneer on a fault surface with a later zeolite overprint and late quartz (Qtz)-calcite (Cal 2) infill. E) Zeolite (Zeo) veins cross-cutting early calcite (Cal 1) and epidote (Epi 3) veins. F) Deformed early calcite veins (pale brown coloured) (Cal 1) being cross-cut by translucent white late quartz-calcite vein (Cal 2). A-F) Scratch pen for scale = 13cm, B) Scale bar arrow = 10cm.

Prehnite veins, significantly less abundant than epidote veins, occur in drill holes BH1 and BH2 together with epidote. Prehnite is commonly pale grey-green in colour, and infills veins, belonging to dense networks grading to proper dilatant hydraulic breccias (Figure 4A – drill core). In the case of the hydraulic breccias, included fragments are either host rock fragments of polycrystalline aggregates of quartz-feldspar or reworked epidote cataclasites/veins (in places with host rock fragments with included veins; Figure 5C).

The earlier epidote locally forms the matrix mineral of at least two generations of cataclasite to ultracataclasite, associated with discrete NE-SW to ENE-WSW-striking slip planes that dip from shallowly to sub-vertically (20°-85°). The earliest epidote cataclasite to ultracataclasite (epi 1) is typically only preserved as isolated fragments 1-5 mm in size and may have originally formed thin discrete pockets with a weak to distinct foliated to banded matrix dominated by very fine-grained epidote and clay (forming up to 75 %-90 % of the pockets). The included clasts are fine-grained (average size <60 µm), poorly sorted and subangular, and are typically mono to polycrystalline aggregates of quartz-feldspar host rock (Figure 5D). The second generation of epidote cataclasite (epi 2) occurs as localised zones (typically <10 cm in width), with a massive matrix (making up 60 %-70 % of the zones) formed by fine-grained epidote and clay (Figure 5A & B). The included fragments are very fine to coarse-grained (10 µm-6 mm), poorly sorted, angular to sub-angular, and polycrystalline fragments of host rock (quartz-feldspar) or reworked fragments of the earlier epidote ultracataclasite. The included epi 1 and host rock fragments within the epi 2 cataclasite exhibit minor offset and rotation from each other, suggesting that there was limited to no rigid-body rotation and mechanical comminution of the fragments.

Rarely, prehnite ultra-cataclasites occur as discrete zones 3-5 cm in width, striking NNW-SSE and NW-SE, and dipping shallowly to moderately (30°-65°), with the prehnite matrix forming >90 % of the zones. Overall, they are very fine-grained, with interspersed clay. The included clasts are fine-grained (<50 µm-1 mm), moderately sorted, subrounded to angular, and made up of mono to polycrystalline fragments of host rock and epidote cataclasite. The prehnite ultracataclasites are associated with the epidote cataclasites, with both the cataclasites mutually reworking one another.

4.2.2 D_2: repeated sericite-chlorite-calcite-stable faulting

D_2 sericite-chlorite-calcite shear features (Figure 4) invariably rework D_1 structures. They strike on average NE-SW or, subordinately, NW-SE, E-W, and NNE-SSW (Figure 6), and dip variably between ~35° and ~75°. These structures are

https://doi.org/10.5194/egusphere-2023-2504
Preprint. Discussion started: 8 November 2023

commonly strike- to oblique-slip faults, although thrusts and normal faults also occur, commonly associated with shallower features.

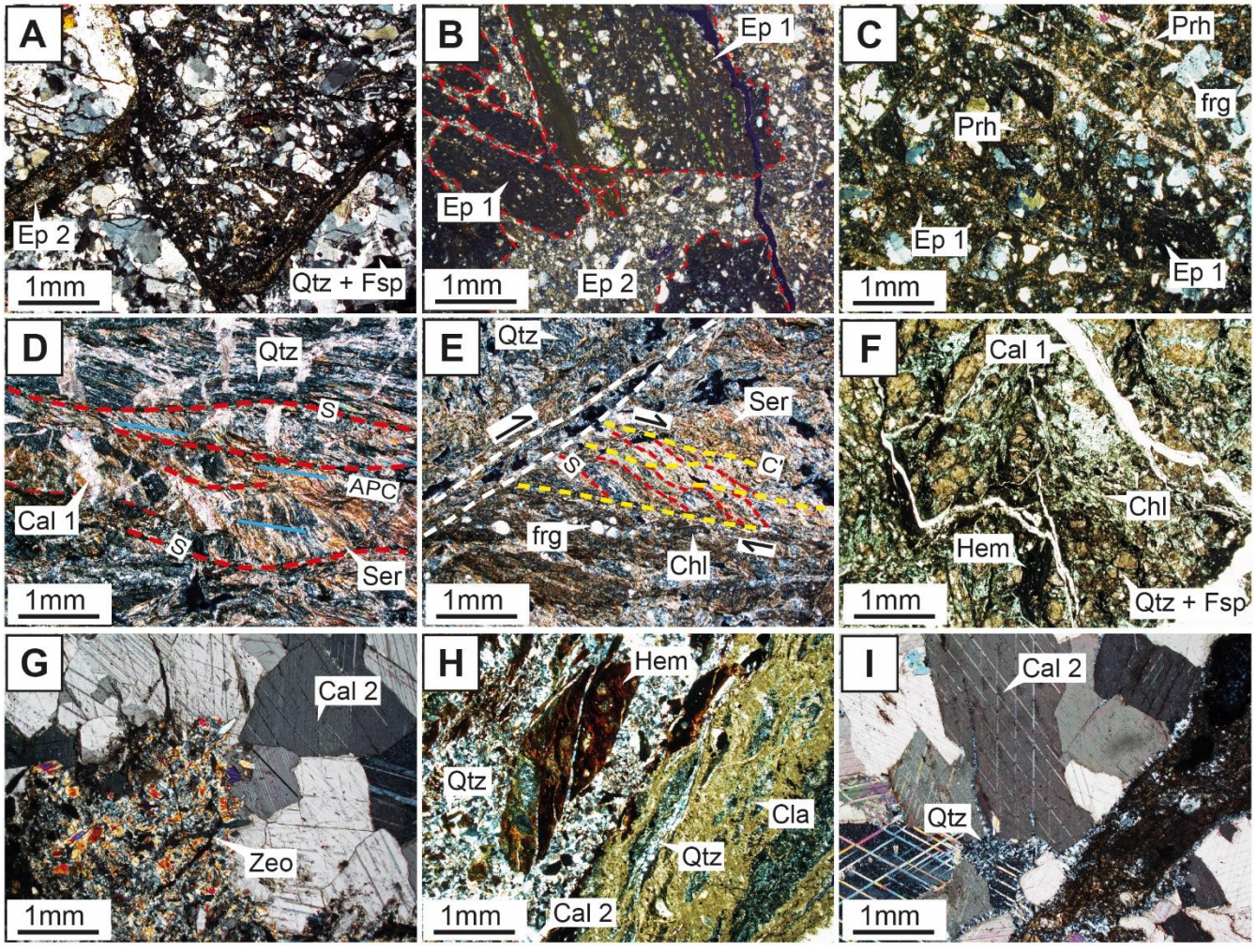

Figure 5. Photomicrographs outlining the progressive deformation episodes affecting Smøla over time. A) An Ep 2 vein and cataclasite reworking host rock monzogranite; B) Two generations of light green epidote cataclasites, an earlier ultracataclasite (Ep 1) fragments, almost isotropic, banded to foliated (yellow dashed lines highlighting the foliation), set within a later cataclasite (Ep 2). C) Prehnite (Prh) hydraulic breccia and veins reworking Ep 1 cataclasite/veins and host rock fragments. D) Asymmetric folds in a sericitic fabric, and early calcite veins. Associated with the folds, a rootless axial planar cleavage has formed (blue lines), along which a later foliation (red lines). E) Possible ECC fabric reworking the fabric since in D, forming in a sericite-chlorite shear zone. C'-planes (yellow lines), associated to chlorite, have formed inclined to a main shear surface (white line), and are reworking and back-rotating the cleavage-related foliation (from D), forming S-surfaces. Reworked host rock fragments are also present associated with the C'-planes, and chlorite. F) Chlorite-hematite breccia to gouge with deformed early calcite veins (Cal 1), and highly altered host rock minerals (feldspars). G) Zeolite-calcite (+/- interstitial hematite in the zeolite) vein, with the zeolite crystals subhedral to euhedral crystal faces within the calcite. Overall, the vein is relatively undeformed. H) Hematite indurated gouge reworked by a later quartz-calcite vein. Abundant clays are adjacent to the vein. I) Late quartz-calcite vein (Cal 2), exhibiting low deformation in the form of calcite twinning. All photomicrographs are 2.5x, XPL, except for F, which PPL.

https://doi.org/10.5194/egusphere-2023-2504
Preprint. Discussion started: 8 November 2023

These structures occur as single shear fractures or dense networks and some brittle-ductile shear zones. The well-developed deformation zones, with locally foliated gouge with highly fractured and disaggregating host rock clasts and early deformed calcite veins (Figure 4C), typically strike from NE-SW to E-W, and dip at either 15°-20° or sub-vertically. D2 structures, especially the well-developed deformation zones, are almost phyllitic at the microscale (Figure 5D & E), locally involving fine to medium-grained sericite/muscovite (30-40 %), chlorite (30 %), and clay (>5 %), with elongate domains of fine-grained recrystallised quartz (>20 %; the matrix forms ~80 % of the total volume). The host-rock clasts included within this groundmass are 20 µm-1 cm monocrystalline quartz fragments or polycrystalline aggregates of quartz and altered feldspar with subrounded shapes.

Microstructural relationships indicate at least two distinct deformation events: an early event with localised shearing along axial planar cleavages in an early folded sericite groundmass with calcite veins (Figure 5D); a subsequent event, which involved the reworking and rotation of the earlier axial planar cleavage shear planes (S-surfaces) by later C'-planes. This resulted in the development of an extensional crenulation cleavage (ECC) -type fabric (Figure 5E). These ECC zones also rework D1 epidote cataclasite and fragmented host rock. The host rock fragments locally form σ porphyroclasts with very fine-grained quartz in the strain shadows, and the sericite and chlorite groundmass (and very fine-grained clay) deflected around them.

4.2.3 D_3: chlorite-hematite-decorated fault rocks and shear fractures

The D_3 chlorite-hematite structures (Figure 4D), trend generally NE-SW with a subordinate NNE-SSW trend (Figure 6). The D_3 structures dip variably, although mostly steeply (~85°). Kinematically, most of the D3 structures are either tensile features or shear fractures accommodating top-to-the ENE/WSW and NNW normal to oblique-normal faulting.

Brown-red staining or 'dusting' of hematite and chlorite decorate and infill these structures. D_3 structures occur as individual anastomosing shear fractures, which locally have hematite slickensides, grading to networks, and breccias and gouges (and possible cataclasite or indurated gouge). The chlorite-hematite breccias to gouges are typically diffuse zones (up to ~3 m thick), with abundant D_3 fractures forming damage zones around them. The gouges are on average moderately to well consolidated features in hand specimen (Figure 4D).

The breccia and gouge at the microscale are cemented by chlorite (40 %), hematite (30-50 %), and clay (10-20 %), with the matrix forming 5-20% of the overall zones (rarely up to 60 %; Figure 5F). The chlorite grains are either overprinting or have grown between the fragmented host rock (and host rock clasts), forming elongate grains in places. The hematite cement is dark red-brown to opaque in PPL, with the staining/ 'dusting' occurring as very fine-grained particles within fractures/matrix and overprinting the host rock. The host rock clasts themselves are typically medium to coarse-grained in size (2 mm-1 cm), moderately to poorly sorted, clast-supported, and comprised by altered quartz-feldspar (feldspar is partially altered to sericite) polycrystalline fragments. Elsewhere, the D_3 structures are associated with thin pockets of hematite-rich foliated to banded cataclasite/indurated gouge (<2 cm in thickness; Figure 5H), with a very fine-grained matrix (up to 80% of the zone) comprised

https://doi.org/10.5194/egusphere-2023-2504
Preprint. Discussion started: 8 November 2023

of hematite (80%), clay (15%), and chlorite (5%), with incorporated fine-grained (20-600 µm), poorly sorted and sub-rounded host rock clasts.

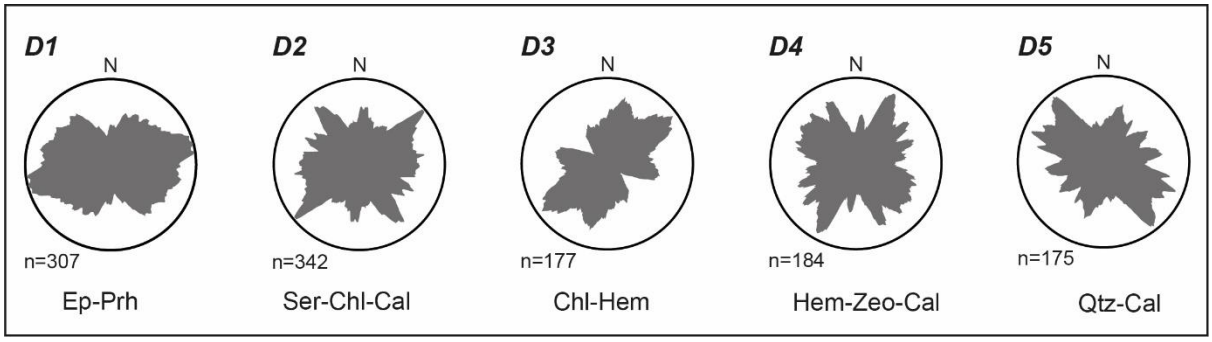

Figure 6. Rose plots showing strike orientation trends (frequency) of deformation features in outcrop and drill core, sorted by deformation episode D1 to D5, associated with coeval mineral assemblages. Mineral types: Ep=epidote, Prh=prehnite, Ser=sericite, Chl=chlorite, Cal=calcite, Hem=hematite, Zeo=zeolite, Qtz=quartz

4.2.4 D_4: hematite-zeolite-calcite veining

The D_4 hematite-zeolite-calcite structures (Figure 4E & F), which crosscut the earlier epidote, sericite-chlorite-calcite (clc 1) and chlorite-hematite structures, possess variable strike orientations. Most frequently are the NE-SW striking features, with subordinate more diffuse trends also discernible, involving NNW-SSE to WNW-ESE orientation trends (possibly forming orthogonally to the NE-SW trend) (Figure 6). The D_4 structures dip variably, but overall, mostly at ~70° (although a significant portion dip at ~30°).

The D_4 hematite-zeolite-calcite structures are mostly tensile veins (0.1-6 mm in thickness), which are pervasive across Smøla (Figure 4E & F – drill core), with other more rare examples of hydraulic breccias and shear fractures with slickenside surfaces also present. Along with zeolite, the hematite component typically occurs as a bright-red type, different from the D3-related hematite, with a later less deformed type of calcite (clc 2) (Figure 7). In outcrop and in drill core, D_4 structures most commonly occur as coarse-grained 'sugary' masses of zeolite-calcite, locally mineralising over pre-existing veins of epidote or chlorite-hematite (Figure 4E).

At the microscale, the D_4 veins are comprised by zeolite (laumontite) occurring as fine to medium-grained decussate subhedral prismatic crystals, in places with interstitial Fe staining. In the places where zeolite crystals have intergrown with late calcite, they form bounding comb-type textures with euhedral crystal morphologies (Figure 5G). Additionally, radial masses of zeolite occur as grain boundary growths within the calcite portions of the veins, indicating the coeval mineralisation of both minerals. The zeolite, hematite, and late calcite (clc 2) components in these veins show little to no significant post-crystallisation deformation implying the D_4 veins are indeed relatively late.

https://doi.org/10.5194/egusphere-2023-2504
Preprint. Discussion started: 8 November 2023

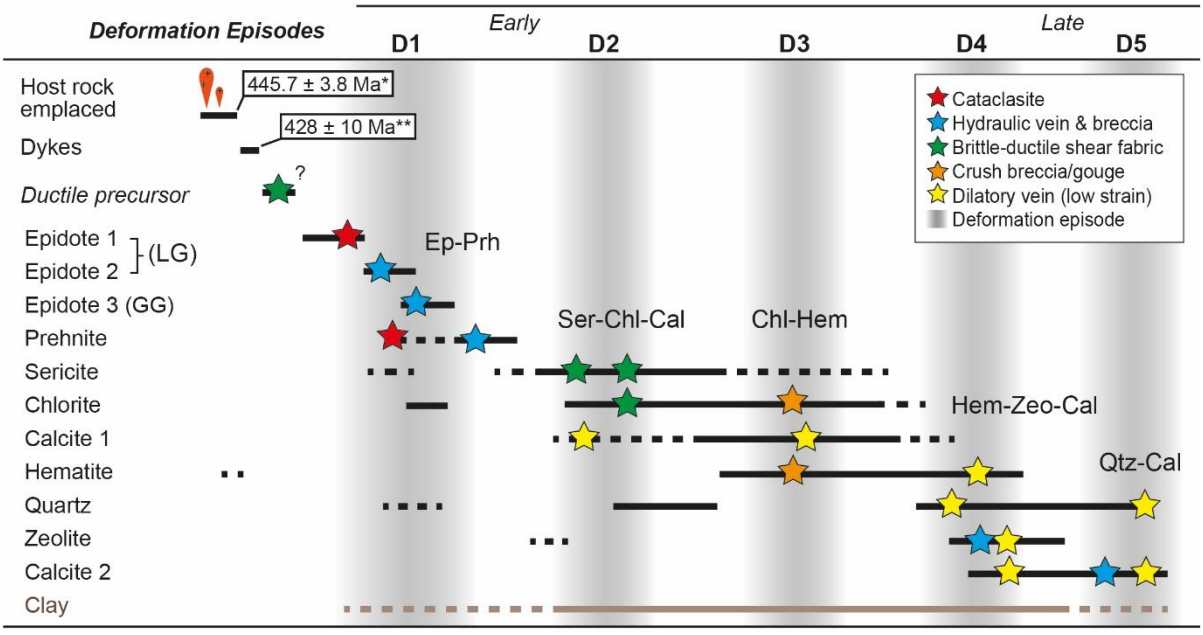

Figure 7. Chronological table of showing relative mineralisation times of different mineral coating types, key deformation features associated with each mineral type is shown in relative chronology, with clustering of mineralisation and deformation features grouped into five main deformation episodes. Duration of possible authigenic clay mineralisation is also shown relative to the other mineral phases. These episodes are associated with specific mineral assemblages. Mineral types: Ep=epidote, Prh=prehnite, Ser=sericite, Chl=chlorite, Cal=calcite, Hem=hematite, Zeo=zeolite, Qtz=quartz. *Host rock age provided by (Tucker et al., 2004)**; ****Age of dyke emplacement by** Gautneb (1988)**.**

4.2.5 D_5: quartz-calcite veining

The D_5 quartz-calcite veins, involving the late calcite variety (Cal 2) and mineralised quartz, rework and offset all other deformation features (D_1 to D_4) (Figure 7). These features are most frequently NW-SE striking, with subordinate trends oriented WNW-ESE and NNE-SSW (Figure 6). Overall, these veins have moderate dips (~30°-70°) on average. Most of these features are either tensile veins or extensional features with normal slip-sense.

The D_5 quartz-calcite veins, in outcrop or intersected in drill core, are translucent to opaque white, exhibit crack-seal layering parallel to the vein-host boundary and are planar to bifurcating features (Figure 4F). The veins occur as singular narrow to wide veins (0.1 mm-22 cm) or as complex vein networks, and in places, hydraulic breccias with included angular fragments of the host rock. Commonly, these late veins are within and subparallel to existing deformation features, such as sericite-chlorite deformation zones, and may represent a later tensile reactivation of these features (the earlier features being mechanically weak planes within the host rock volume) (Figure 4D). The late quartz-calcite veins crosscut the earlier calcite veins (clc 1; Figure 4F), which are less quartz-rich, relatively massive, more opaque white and possess deformed non-planar morphologies to disaggregated irregular domains (for example in D2).

https://doi.org/10.5194/egusphere-2023-2504
Preprint. Discussion started: 8 November 2023

At the micro-scale, the D_5 veins contain medium to coarse-grained calcite crystals, typically anhedral, exhibiting distinct cleavage, with fine-grained quartz grain rims along the borders or between the calcite grains (Figure 5I). In places, the quartz is coarser-grained, forming comb-type textures with euhedral crystal terminations into the larger calcite crystals. Commonly, quartz and calcite also mineralise as alternating bands parallel to the vein border, indicating multiple crack-seal mineralisations. Although these veins are not significantly deformed after mineralisation, similarly as D_4, the calcite in the veins is twinned, suggesting the veins have experienced later strain.

Two zones do not correlate over the drill holes: in BH1 an NNE-SSW striking, moderately SE-dipping zone involving D_2 chloritic and sericite cataclasite and gouge with a massive late quartz-calcite vein; and in BH2, an ENE-WSW striking, shallowly S-dipping zone (90.58 m-91.37 m) made up of a D_3 chlorite-hematite breccia to gouge with an associated alteration zone.

Where possible, these different intersected zones in BH1 and BH2 could therefore be linked by modelled tabular 3D volumes representative of structures, as shown in Figure 10A (with downhole zones labelled Zone 1 to 4). The structures are modelled through a volume set around the two drill holes (150 x 225 x 260 m in size), which being a local representation, is not large enough to characterise Smøla. The zones crosscut each other, without significant offsets (assumed to be negligible for this modelling exercise), with the zones typically between 1 m to 6 m in true thickness, with some dip and thickness variation (pinch and swell) through the modelling volume based on the drill hole intersections (N-S and E-W sections in Figure 10A). The zones indicate various orientation trends, with the D2-related volumes being moderately south to SE-dipping, while the D3-related are relatively shallowly-dipping zones.

To explore the multiscalar nature of the Smøla deformation features, 3D models of selected intervals of D_5 quartz-calcite veins in BH2 (14.6 m x 14 m x 19 m in size), and epidote-prehnite (D_1) veins in BH1 (2.3 m x 2.2 m x 2.3 m in size) were also produced utilising the available structural data for the afore mentioned features (Figure 10B). These models, including Figure 10A, display the 3D network characteristics of brittle deformation features, with either subparallel or inclined structures forming systematic to semi-systematic arrays of structures. From the drill data, the different structures occur at different scales: the D_2, D_3-related structural zones can be modelled at the hundred(s) of metres-scale (Figure 10A), to the tens of metres-scale for the D_4, D_5 veins (Figure 10B), and metres to sub-metre scale for the D_1 structures (Figure 10B). In addition, the structures associated to the various deformation episodes have, on average, different aperture widths and potential strike extents. The D_2 structures have the largest aperture and strike extents, while the D_1 features possess the least structural continuity on average.

Overall, the modelling results provide powerful multiscalar visualisations of the complex structural network arrays that the different deformation features form in 3D space, sorted by deformation episode. As these network geometries are not always appreciable in either outcrop or as drill hole intersections, the various characteristics are instead more apparent once they are

https://doi.org/10.5194/egusphere-2023-2504
Preprint. Discussion started: 8 November 2023

460 modelled. Although the modelling volumes are limited in size (at all scales), the geometries and morphologies of the different modelled features are representative for rock volumes around the BH1 and BH2 drill holes at least and define geometries that can easily be up-scaled, also confirming relative crosscutting relationships.

4.3 K-Ar geochronology and X-ray diffraction

Seven fault gouge samples were collected from drill holes BH2 (SK2008, SK2012, SK2015) and BH4 (120714), and fault core
465 exposures at different outcrops on Smøla Island (SK1024_1, SK1029_1, SK1033_1; Table 2 & Figure 8) for dating of authigenic and synkinematic K-bearing clays.

Table 2. Summary of K-Ar samples collected from either drill holes BH2 and BH4, or field stations on Smøla Island.

Sample	Site/BH	Host rock	Orientation (dip/dip direction)	Deformation episode	Description
SK2008	BH2	Monzogranite, fault rock	10/285	D_3	Hydraulic breccia to crackle breccia and hematite-bearing shear veins.
SK2012	BH2	Monzogranite, fault rock	15/320	D_2	Shear foliation within sheared and foliated gouge band.
SK2015	BH2	Monzogranite, sheared mafic?	37/183	D_2	Well milled gouge, some residual veins, and lithic fragments present (possibly from bounding monzogranite).
120714	BH4	Diorite, clays	54/059	D_3, D_4	Friable gouge in shear band, clay rich, with zeolite veins.
SK1024_1	1024	Diorite, fault gouge	73/179	D_2	Sample from upper portion of exposed sub-vertical structure; well developed gouge.
SK1029_1	1029	Monzodiorite, fault gouge	80/166	D_2	Gouge sample, green, chloritic, structure parallel to major E-W structure.
SK1033_1	1033	Gabbro	80/155?	D_3	Possible fault gouge within saprolite zone.

470 The different samples are characterised by comparatively different weight percents (wt%) for potassium (K on Table 3), with the value relating to the amount of potassium-bearing minerals (such as illite, muscovite, or potassic feldspar) in the analysed material. Samples SK2012 and SK2015 possess the highest weight percents, while 120714, SK1024_1 and SK1033 the lowest weight percents. The samples also reported variable radiogenic ^{40}Ar percents, with samples 120714, SK1033_1 and SK1024_1 reporting the lowest percents.

475

The samples yielded ages between 74.7 ± 1.7 Ma and 314.9 ± 5.4 Ma (Figure 9A & *Table 3*), with results commonly following an age spectrum curve with the oldest ages corresponding to the coarsest size fractions and the lowest ages corresponding to the finest size fractions. Sample SK1029_1, however, does not follow this trend, with the oldest age corresponding to the size fraction 0.4-2 µm. This is possibly owing to the amount of zeolite within the 0.4-2 µm (13 wt%), 2-6 µm (21 wt%), and 6-10

https://doi.org/10.5194/egusphere-2023-2504
Preprint. Discussion started: 8 November 2023

480 µm (25 wt%) size fractions (Table 4), with radiogenic ^{40}Ar loss from the zeolite crystal structure, and therefore lower age results. As the coarser size fractions may involve 'mixed' results of both authigenic and protolithic K-Ar signals (Viola et al., 2016), the ages associated with the finest size fractions are considered the most reliable as they potentially record the last deformation episode archived in the dated fault rock.

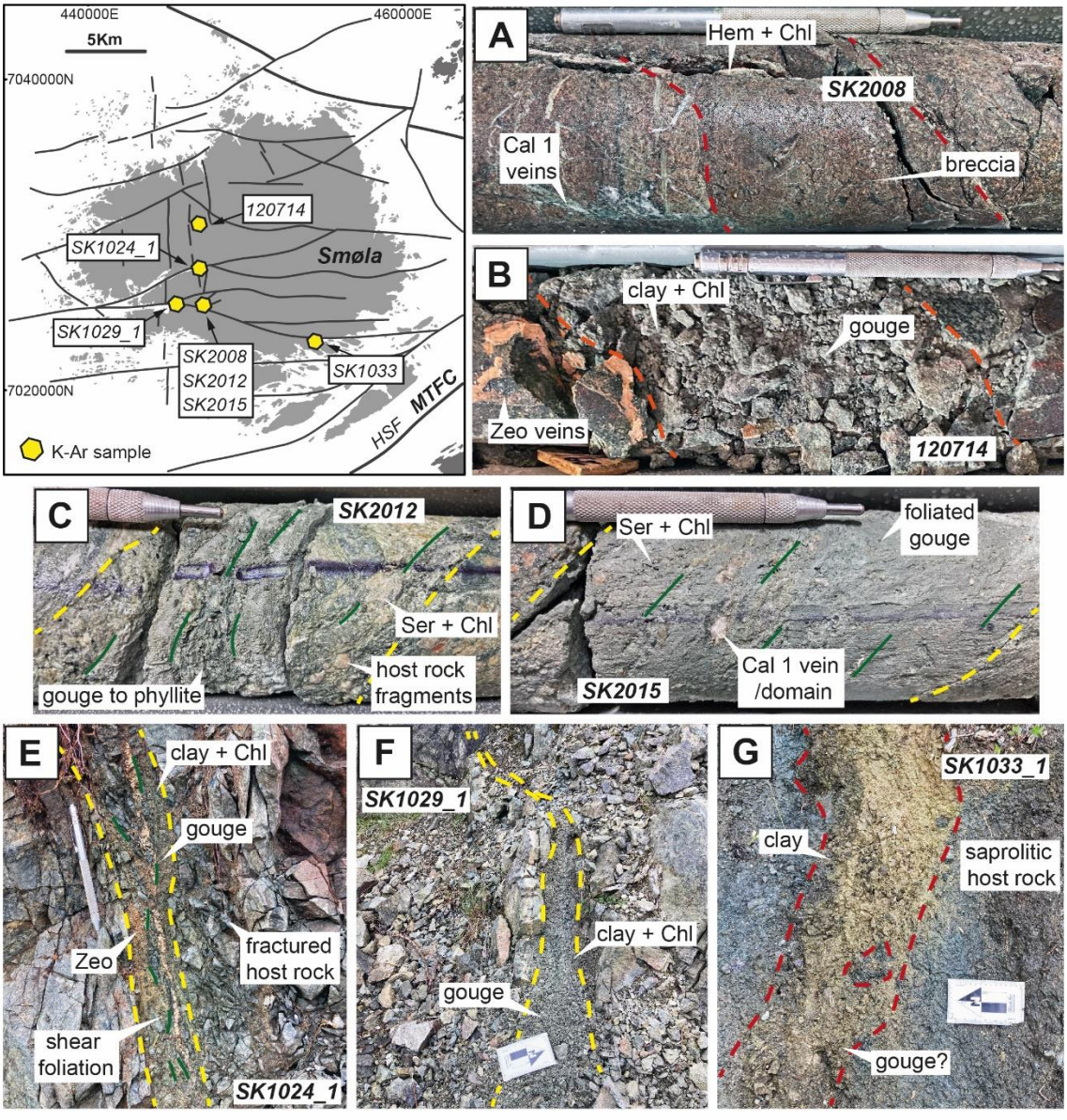

485 **Figure 8. The locations on Smøla Island of the collected K-Ar samples relative to mapped lineaments, and A-G) K-Ar sample sites, with samples SK2008, SK2012, and SK2015, 120714 collected from diamond drill core, and samples SK2024_1, SK1029_1, and SK1033_1 collected from field locations. Scratch pen for scale = 13cm, or scale bar arrow = 10cm.**

https://doi.org/10.5194/egusphere-2023-2504
Preprint. Discussion started: 8 November 2023

Table 3. K-Ar analysis age data results of the Smøla samples by size fraction.

	Sample		40Ar*			K			Age Data	
	Fraction (µm)	Mass (mg)	mol/g	σ (%)	40Ar* %	Mass (mg)	wt %	σ (%)	Age (Ma)	σ (Ma)
SK2008	<0.1	2.088	2.894E-10	0.57	40.4	50.6	1.63	1.76	99.6	1.8
	0.1-0.4	2.036	3.821E-10	0.54	53.9	51.6	1.46	1.78	144.9	2.6
	0.4-2	2.096	6.728E-10	0.50	77.2	52.8	1.79	1.74	204.7	3.5
	2-6	3.604	1.161E-09	0.46	89.6	52.2	3.06	1.64	206.5	3.3
	6-10	2.672	1.376E-09	0.47	94.7	51.0	3.85	1.58	195.2	3.1
SK2012	<0.1	2.016	2.065E-09	0.49	90.3	51.0	5.75	1.43	196.1	2.8
	0.1-0.4	3.654	2.221E-09	0.46	92.4	52.0	5.46	1.44	220.5	3.1
	0.4-2	2.938	2.716E-09	0.46	95.6	52.8	5.40	1.44	268.9	3.8
	2-6	2.524	2.536E-09	0.47	98.3	50.9	4.50	1.53	298.8	4.4
	6-10	2.452	2.106E-09	0.47	98.6	50.9	3.85	1.58	290.7	4.4
SK2015	<0.1	2.596	2.036E-09	0.47	90.4	51.5	5.51	1.44	201.4	2.9
	0.1-0.4	3.048	2.202E-09	0.46	93.1	51.3	5.33	1.46	223.7	3.2
	0.4-2	3.122	2.522E-09	0.46	95.5	51.6	5.16	1.47	261.8	3.8
	2-6	3.612	1.832E-09	0.46	97.0	51.1	3.37	1.62	289.1	4.5
	6-10	2.466	1.370E-09	0.47	98.4	50.9	2.54	1.69	287.0	4.7
120714	<0.1	2.750	5.869E-11	1.24	8.2	50.7	0.44	1.91	74.7	1.7
	0.1-0.4	1.368	1.122E-10	1.26	14.5	50.7	0.58	1.90	109.0	2.4
	0.4-2	3.600	1.844E-10	0.47	28.8	50.8	0.77	1.88	132.6	2.5
	2-6	2.710	2.786E-10	0.45	51.6	50.1	1.11	1.85	138.8	2.5
	6-10	2.554	3.933E-10	0.42	51.0	52.6	1.41	1.82	153.6	2.7
SK1024_1	0.1-0.4	2.220	1.982E-10	0.58	42.3	50.5	0.67	1.92	162.1	3.1
	0.4-2	1.600	3.118E-10	0.59	31.1	50.4	0.95	1.89	180.5	3.4
	2-6	2.568	3.196E-10	0.45	42.9	52.6	1.00	1.88	176.1	3.2
	6-10	3.186	2.926E-10	0.42	53.2	54.6	0.99	1.88	163.5	3.0
SK1029_1	<0.1	2.618	5.023E-10	0.41	50.4	51.3	1.34	1.85	204.1	3.7
	0.1-0.4	3.728	5.895E-10	0.38	57.3	57.2	1.18	1.85	267.3	4.7
	0.4-2	3.136	9.189E-10	0.38	77.4	56.0	1.54	1.82	314.9	5.4
	2-6	2.582	8.275E-10	0.39	84.9	62.8	1.92	1.76	232.8	3.9
	6-10	1.636	8.246E-10	0.45	88.3	52.5	2.05	1.78	218.2	3.8
SK1033_1	<0.1	2.224	1.814E-11	9.36	0.8	51.7	0.08	1.97	128.1	11.8
	0.1-0.4	2.236	2.085E-11	7.31	0.9	51.4	0.09	1.97	126.0	9.2
	0.4-2	2.854	9.294E-11	1.33	5.0	53.2	0.21	1.96	234.5	5.2
	2-6	3.042	1.020E-10	0.91	9.0	60.3	0.22	1.95	247.2	5.0
	6-10	2.354	1.219E-10	0.98	8.6	54.5	0.25	1.95	263.3	5.4

Samples SK2012 and SK2015 yielded very similar ages for all size fractions even though the sampled fault structures are differently oriented, with SK2012 striking NE-SW (15/320) and SK2015 striking E-W (37/183). Samples 120714, SK2008, and SK1033_1 provided the youngest ages (74.7 ± 1.7 Ma, 99.6 ± 1.8 Ma, and 128.1 ± 11.8 Ma respectfully) for the finer fractions (<0.1 µm and 0.1-0.4 µm), with the remaining samples (except for SK1024_1) returning an age around 200 Ma for

https://doi.org/10.5194/egusphere-2023-2504
Preprint. Discussion started: 8 November 2023

the finest fraction. Overall, the results show size fraction age clustering, particularly the finest and coarsest fractions, around ~100 Ma, 200 Ma, and 300 Ma (Figure 9A).

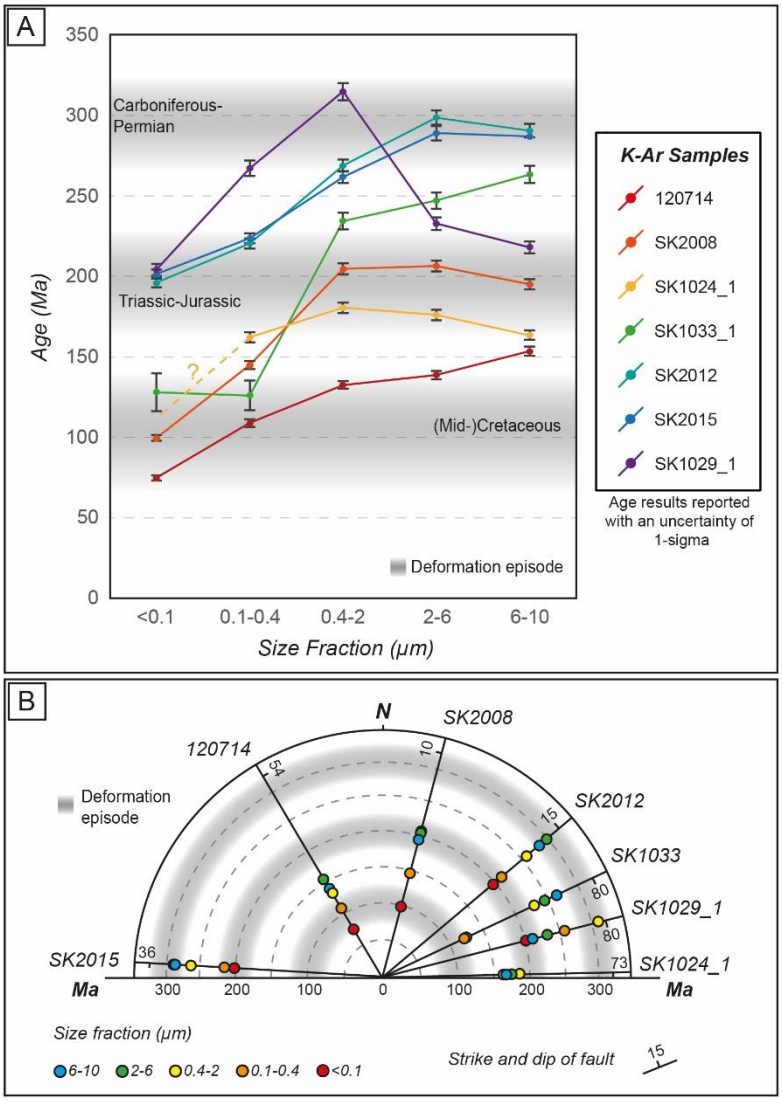

Figure 9. A) K-Ar age spectra results for the seven samples. Data is expressed by size fraction of the sampled medium against determined age, with age clustering indicating possible authigenic (and deformation) episodes; B) Radial plot showing dated samples with K-Ar ages and size fraction (coloured circles) plotted on lines indicating the orientations of sampled structures.

Plotting age results by size fraction and structure orientation (Figure 9B), one can appreciate that the NNE-SSW and ENE-WSW samples both yielded the youngest ages in the Late Triassic-Early Jurassic to Mid-Cretaceous (~200 Ma – 100 Ma), while the NE-SW and WNW-ESE oriented structures yielded ages between the Late Carboniferous and Late Triassic/Early

https://doi.org/10.5194/egusphere-2023-2504
Preprint. Discussion started: 8 November 2023

Jurassic (~300 Ma – 200 Ma). The oldest ages from the coarsest fractions are both associated from fault rocks from NE-SW and ENE-WSW structures.

Table 4. X-ray diffraction results for the K-Ar samples. Mineral abbreviations: Qtz = quartz, Ksp = Potassic feldspar, Plg = plagioclase, Ill/mus = illite/muscovite, Chl = chlorite, Smc = smectite, Hem = hematite, Cal = calcite, Zeo = zeolite, Amp=amphibole. Note that due to very poor crystallinity and/or the lack of structural data for mixed-layer clay minerals, only semi-quantitative assessments could be made. Wt % amounts are represented by x=<5, xx = 5-15, xxx = 15-30, xxxx = >30. NEM = Note enough material.

Sample	Fraction (µm)	Qtz	Ksp	Plg	Ill/mus	Chl	Smc	Chl/chl-smc	Hem	Cal	Zeo	Amph	Other
SK2008	<0.1				Trace	xx	xxxx						
	0.1-0.4				xxx	xxx	xxxx		x				
	0.4-2	x			xxx	xxxx	xxxx		x				
	2-6	xx	xx		xxx	xxx	xxx		x	x			
	6-10	xx	xx		xxx	xxx	xxx		x	x			
SK2012	<0.1				xxxx	xxx	xx						
	0.1-0.4				xxxx	xxxx	xx						
	0.4-2	x			xxxx	xxxx	xx						
	2-6	xxx			xxxx	xxx	x						
	6-10	xxxx			xxxx	xxx	x						
SK2015	<0.1				xxxx	xxx	xx						
	0.1-0.4				xxxx	xxxx	xx						
	0.4-2	x			xxxx	xxxx	xx						
	2-6	xxxx	x		xxx	xxx	xx			Trace			x?
	6-10	xxxx	x		xxx	xx	x			Trace			x?
120714	<0.1 *						xxxx						
	0.1-0.4				Trace	x	xxxx						
	0.4-2					xx	xxxx			Trace			
	2-6		x	x	x	xxx	xxxx			Trace			
	6-10		x	x	xx	xxx	xxxx			Trace			
SK1024_1	<0.1	NEM											
	0.1-0.4 *	x			Trace?	xxxx	xxxx				Trace		
	0.4-2	xx			Trace	xxxx	xxxx				xx		
	2-6	xx			Trace	xxxx	xxx				xxx		
	6-10	xx			Trace?	xxxx	xxx				xxx		
SK1029_1	<0.1							xxxx					
	0.1-0.4				xx			xxxx			Trace		
	0.4-2	Trace		Trace?	xx			xxxx			xx	Trace?	
	2-6	x		Trace	xx			xxxx			xxx	Trace	
	6-10	x		Trace	xx			xxxx			xxx	Trace	
SK1033_1	<0.1						xxxx						
	0.1-0.4						xxxx						
	0.4-2					Trace	xxxx						
	2-6					Trace	xxxx						
	6-10				Trace	Trace	xxxx						

As shown in Figure 8, and documented by the X-ray diffraction (XRD) results in Table 4, the sampled faults have variable rock textures and compositions: Sample SK2008 (Figure 8A), involves a chlorite-hematite-rich breccia, with significant

https://doi.org/10.5194/egusphere-2023-2504
Preprint. Discussion started: 8 November 2023

amounts of smectite and illite, mostly responsible for the potassic content. Potassic-feldspar content, potentially derived from the host rock, is restricted to the coarser size fractions (2-6 µm and 6-10 µm), limiting the possibility of contamination in the finest size fraction. Both samples SK2012 and SK2015 (Figure 8C & D), being phyllitic to foliated gouge intervals dominated by illite/muscovite (sericite), chlorite, and lesser amounts of smectite, with SK2015 possessing very low amounts of potassic-feldspar in the coarser size fractions (derived from the host rock). Overall, the two samples are structurally and mineralogically similar. Samples 120714 (Figure 8B), and SK1024_1 (Figure 8E) are mostly chlorite and smectite, with traces of illite/muscovite(sericite). However, the presence of zeolite veins within these zones (for 120714 not detected in the XRD results) in the drill core and field, is noteworthy. The sample SK1024_1 lacked enough finest fraction (<0.1 µm) material to be K-Ar analysed, and therefore is only included for demonstrative purposes. SK1029_1 (Figure 8F) is similar to both SK2012 and SK2015, with a composition dominated by sericite and chlorite/smectite. The presence of zeolite, as mentioned before, has influenced the age reporting in the coarser fractions. SK1033_1 (Figure 8G), which is a possible weathered gouge within a saprolite horizon, bound by chloritic slickenside surfaces adjacent to the zone, is dominated by smectite, with only trace amounts of both illite/muscovite and chlorite. The colouration and mineral compositions suggest that this potential structure may be similar to either samples SK2008 (apparently lacking hematite) or SK2012/SK2015.

4.4 Basement deformation in 3D

Outcrops typically offer a 2D view of the deformation features and internal structure of a given rock volume. Utilising the four oriented drill holes (Figure 3, with locations on Figure 1B) we can additionally provide a 3D view of the Smøla geology. Using the Leapfrog Works (Seequent, 2022) 3D modelling software, logged downhole intersections of relevant deformation features and selected orientation data, explicit hanging wall and footwall boundaries were defined within selected rock volumes. Implicit 3D volumes were thus generated constraining the true thickness and orientation of the relevant structures. In the case of BH1 and BH2, modelled structures that extend through more than one drill hole provide insights into the strike continuity and extent of these deformation zones, and the potential fracture connectivity within the Smøla rock volume. Therefore, 3D modelling of drill hole data is a valuable tool in furthering our understanding of rock volume characteristics. Furthermore, as we can incorporate both relative (deformation episodes outlined above, in Figure 7) and absolute deformation ages (also see above), the modelling also includes the temporal dimension.

As drill holes BH1 and BH2 are proximal together, features can be successfully matched between them, and modelled. These drill holes intersected deformation zones, highly fluid-altered and veined intervals, and shear zones/fault cores (Figure 3). Considering the geological and deformation characteristics of each of these zones, particularly the fault core intersections (assumed to have the greatest strike continuity) and the associated damage zones, we can interpret correlations between these different zones. These correlations are also guided by the orientations of bounding deformation features around the fault cores (such as shear fractures) helping to resolve the complete geometries of these zones.

https://doi.org/10.5194/egusphere-2023-2504
Preprint. Discussion started: 8 November 2023

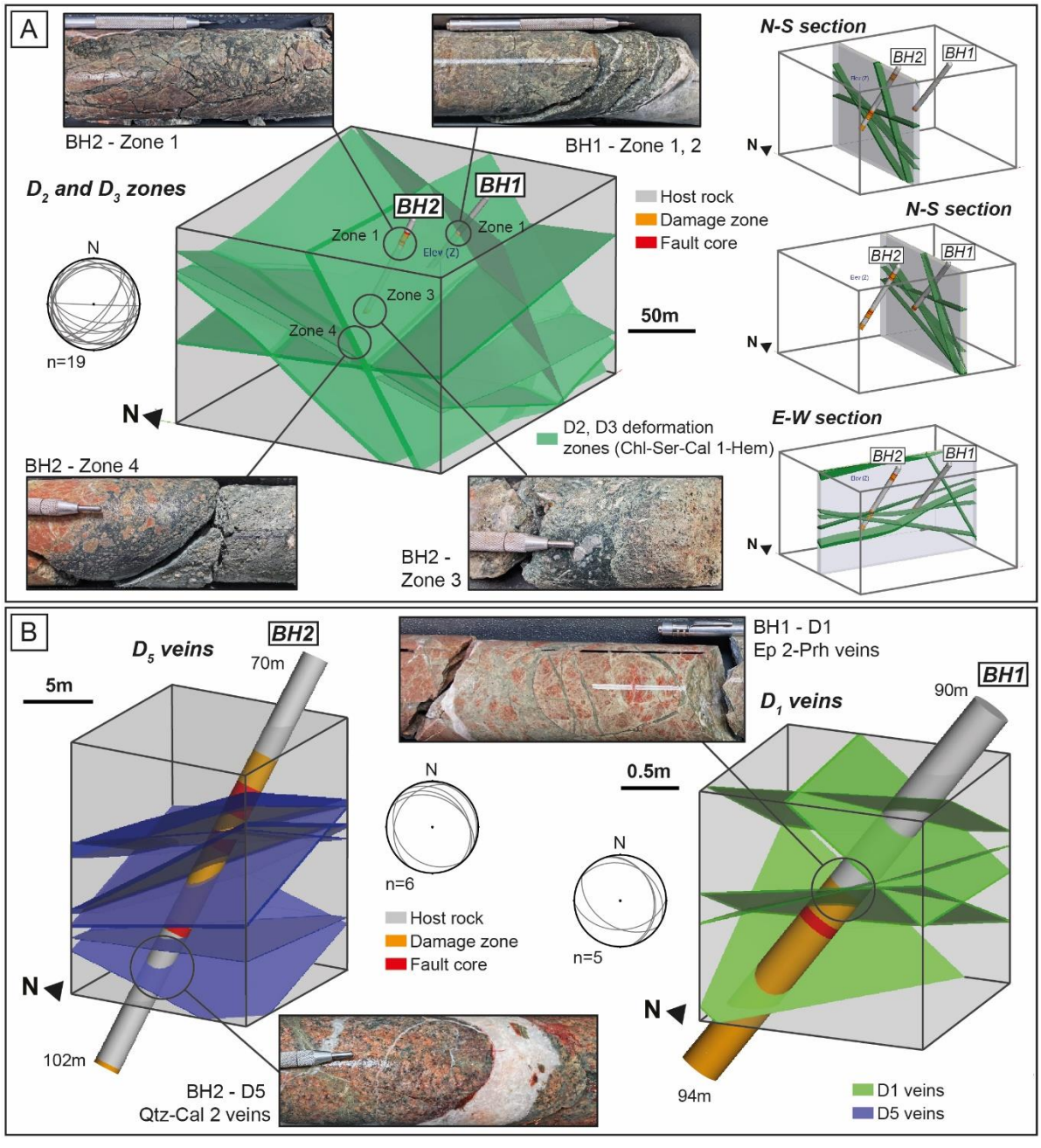

Figure 10. A) 3D model of major intersected brittle structures (green planar volumes) in drill holes BH1 and BH2. Modelling completed in Leapfrog using bounding deformation features, such as shear fractures (plotted in included stereonet). Zones 1 to 4 are representative of the D3-D4 deformation zones present in one or both the drill holes, descriptions include in the text. N-S and E-W cross sections included on the right of the figure, with the N-S sections taken through each drill hole. B) 3D models at different scales to A, with both quartz-calcite (D5) and epidote-prehnite (D1) modelled from drill core structures (included in associated stereonet plots).

https://doi.org/10.5194/egusphere-2023-2504
Preprint. Discussion started: 8 November 2023

Accordingly, between BH1 and BH2 there are at least four correlated zones (Figure 10A): I) In BH1, a shallow E-W, moderately south-dipping zone (37.46 m-37.81 m) that is similarly intersected in BH2 (12.94 m-23.59 m), characterised by an early D1 epidote veins and hydraulic breccia (epi 2) which is cross-cut and reworked by a D_2 chloritic/sericitic breccia, discrete fractures, and D_5 quartz-calcite veins (clc1 and clc 2); II) a zone in BH1 (70.6 m-70.77 m), striking NE-SW and NW-dipping (relatively flat-lying) which widens in BH2 (79.39 m-81.78 m) involving abundant early D_1 epidote veins, and cross-cutting chlorite, hematite (stronger hematite mineralisation in BH2) D3 breccia to cataclasite with deformed calcite veins (clc 1); III) a lower zone in BH1 (92.03 m-96.33 m) striking NE-SW, and shallowly-dipping, also present in BH2 (83.33 m-84.51 m), characterised by D_1 epidote cataclasite that has been reworked by deformation associated with chlorite and zeolite (zeolite is in places limited to the host rock fragments); these cataclasites and breccias are cross-cut by D_4 zeolite-calcite and abundant late D_5 quartz-calcite veins locally forming a dense vein network; and IV) a moderately to shallowly SW-dipping zone, mostly intersected in BH2 (108.08 m-111.1 m) characterised by intensely sheared D_2 sericite-chlorite gouge and phyllitic bands with a broader damage zone of sericite and chlorite fractures, which is also intersected at the base of BH1 (96.57 m-99.24 m).

5 Discussion

5.1 Polyphase evolution of Smøla and the passive margin

Based on our new multiscalar and multi-technique results, we now propose a tectonic history for Smøla and elaborate on the bigger-scale implications on the evolution of the passive margin.

The D_1 epidote-prehnite mineralisation, although not directly dated in this study, has been shown in other areas of the Norwegian margin to have formed from syn- to post Devonian times down to until ~290 Ma (Indrevær et al., 2014; Seranne, 1992; Sherlock et al., 2004; Watts et al., 2023). The D_1 brittle structures (Figure 4A, B, & Figure 10B) rework primary host rock features, and are systematically offset by the D_2 to D_5 structures, indicating that epidote and prehnite mineralised early, as incipient features, after the emplacement of the SHB rocks and dykes, and prior to all other subsequent deformation episodes (Figure 7).

These features can be related to regional-scale D_1 lineaments, oriented NW-SE to NNW-SSE and N-S, which occur over Smøla, the Devonian-aged Edøyfjorden Basin, and the WGR to the SE of the MTFC (Figure 2A & B.I, II, IV, V & Figure 11). Geometrically, these lineaments and structures may have formed during local contraction and folding of the Edøyfjorden Basin during Late-Caledonian extension (Bøe et al., 1989 and Fossen, 2010) (Figure 11). The other D_1 ENE-WSW (varying from NNE-SSW to NW-SE) oriented veins also may represent Riedel shears and tensile veins (veins are mostly orthogonal to the extension opening of the Devonian basins), supporting an association with early brittle sinistral transtension on the MTFC during post-Caledonian extension of the margin (Seranne, 1992; Watts et al., 2023) (Figure 11).

https://doi.org/10.5194/egusphere-2023-2504
Preprint. Discussion started: 8 November 2023

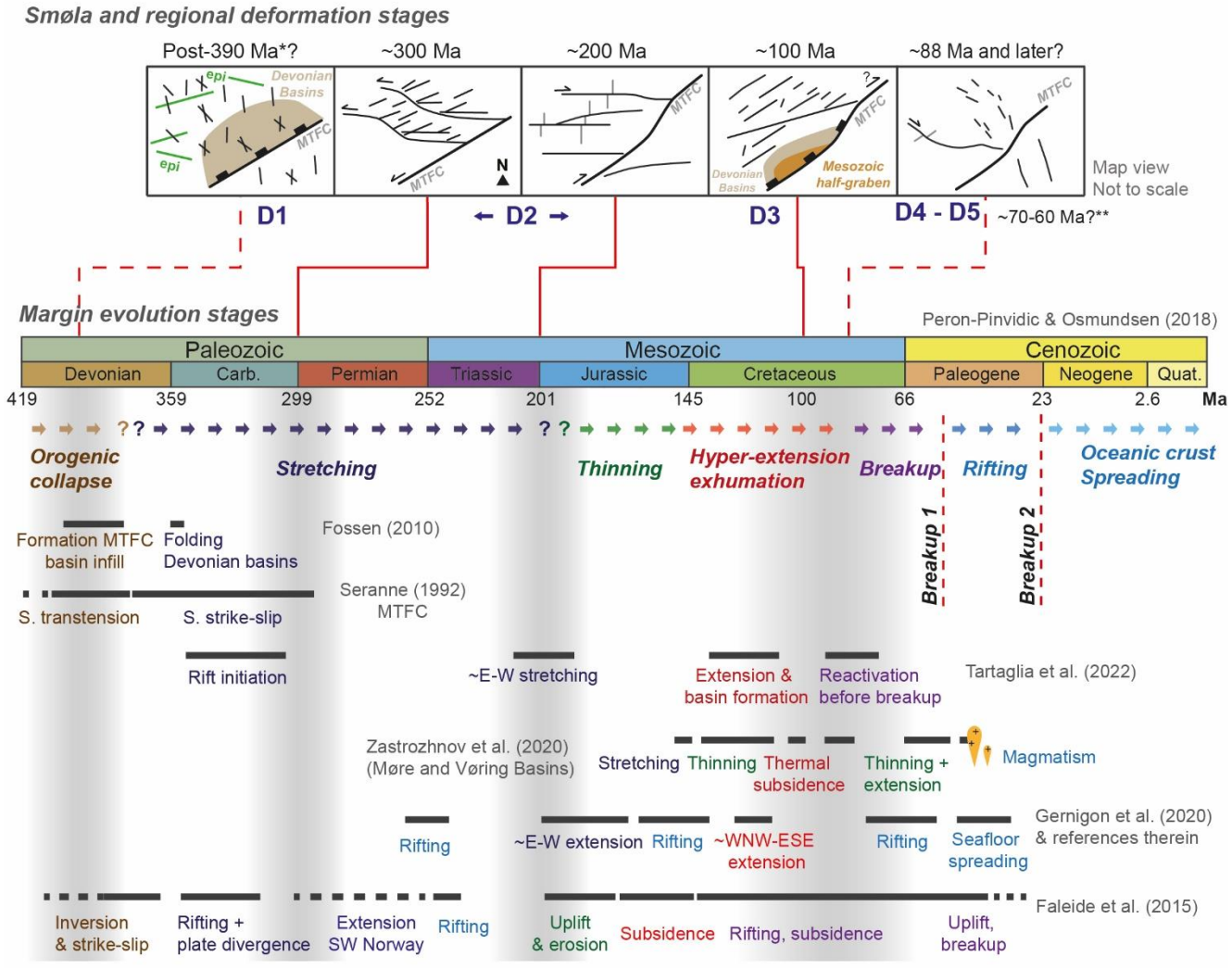

Figure 11. Summary figure integrating this study's results relative to other Mid-Norwegian passive margin evolution studies. The main margin evolution stages are adapted from Peron-Pinvidic and Osmundsen, (2018)**. Ages provided by *** Fossen et al. (2017)**, **** Hestnes et al. (2023)**.**

The D_2 sericite-chlorite-carbonate structures (Figure 4C, and Figure 5D & E), dated to between ~300 and ~200 Ma (Figure 9), are associated with the E-W and NE-SW oriented structures (Table 2, Figure 8C, D, & F). The microstructural and field evidence indicates at least two deformation phases accommodated by these structures. The earlier deformation phase, during the Late Carboniferous-Early Permian, may well be attributed to sinistral strike-slip or transtension conditions along the HSF, as suggested by Seranne, (1992) and Watts et al. (2023). The NNE-SSW to NE-SW lineaments on Smøla also have a similar geometry to the ~N-S extensional faults (Raudtinddalen Fault) off the VF, which have been associated with a similar age and kinematics (Watts et al., 2023).

https://doi.org/10.5194/egusphere-2023-2504
Preprint. Discussion started: 8 November 2023

The D_2 E-W to WNW-ESE 2nd order lineaments and the NE-SW 3rd order lineaments (Figure 2B.I & III) indicate sinistral shear with the NE-SW to NNE-SSW lineaments either sinistral R and R' Riedel shears off the E-W WNW-ESE lineaments (Figure 2B.III). Additionally, the E-W to WNW-ESE 2nd order lineaments may also be synthetic P-shears off the main MTFC trend (Figure 11), which along with rare examples of preserved sinistral shear along the N-S lineaments over these lineaments (Figure 2B.I) supports this kinematic interpretation.

This Late Carboniferous-Early Permian sinistral strike-slip or transtension potentially corresponds to the overall NE-SW crustal stretching and rifting of the margin during that time, which resulted in the formation of Late Palaeozoic basins such as the Froan Basin and Høybakken fault-related basin (Kendrick et al., 2004; Faleide et al., 2008; Peron-Pinvidic and Osmundsen, 2018).

Reactivating many of the same lineaments, and corresponding to later D_2 deformation (Figure 11), the E-W to WNW-ESE and ENE-WSW lineaments cause dextral offsets of the older N-S and NW-SE lineaments and geophysical anomalies (Figure 2B.I & V). This phase is likely to relate to the ~200 Ma ages detected on these D_2 structures, including the ENE-WSW structures. The dextral offsets over the reactivated 2nd order lineaments, and the formation of the ENE-WSW lineaments either as P-shears off the E-W lineaments or as R Riedel shears off the HSF, all imply dextral strike-slip kinematics.

Dextral kinematics has been suggested on the MTFC (primarily on the VF) during the Jurassic by Grønlie and Roberts (1989), with Watts et al. (2023) however suggesting this occurred later during the Late Jurassic/Early Cretaceous on the VF. The dextral strike-slip faulting may be a result of Triassic-Jurassic slab-push forces along the margin focussing on a mechanically weak MTFC and associated structures (including over Smøla) (Pascal & Gabrielsen, 2001; Watts et al., 2023). However, at this time, the margin was experiencing the start of an extensional phase with regional subsidence (Tsikalas et al., 2012; Peron-Pinvidic and Osmundsen, 2018), with commonly ~E-W crustal extension (Gernigon et al., 2020; Tartaglia et al., 2022), which does not fit well with dextral kinematics, suggesting this tectonic phase remains poorly resolved.

The hematite-bearing NNE-SSW and NE-SW oriented structures (Table 2, Figure 8A, G) returned authigenic ages of between ~200 Ma and ~120-100 Ma (Figure 9). These ages correspond to the Triassic-Jurassic dextral strike-slip activity and then Jurassic-Cretaceous dip-slip extension and half-graben development on the HSF, associated with the deposition of the Mesozoic sediment basin sediments (Bøe & Bjerkli, 1989).

Associated with D_3, the pervasive NE-SW, NNE-SSW lineaments (mostly 3rd order) formed after D_1 and D_2, as suggested by the lack of offset across the earlier lineaments. Moreover, differently to D_2, the limited horizontal offsets of magnetic fabric

https://doi.org/10.5194/egusphere-2023-2504
Preprint. Discussion started: 8 November 2023

over the D_3 lineaments suggest these lineaments are predominantly dip- to oblique-slip faults (Figure 2B.V). Many of the D_3 lineaments are subparallel to the trace of the HSF and the axis of the Edøyfjorden Basin, and thus may have developed coevally as the basin stretched further and deepened during the Mesozoic. Hyper-extension and exhumation of the margin during the Jurassic-Cretaceous drove regional rifting and basin development, forming the significant Cretaceous basins (including the Møre and Vøring basins; Figure 11) (Faleide et al., 2008; Peron-Pinvidic and Osmundsen, 2018).

Following this, gentle folding of the Mesozoic basin rocks around N-S oriented fold axes occurred during late D_3 times (Bøe & Bjerkli, 1989). Geometrically, these folds indicate Late Mesozoic dextral transpressional conditions after dip-slip faulting on the HSF, with ~E-W shortening of the basin sediments (Bøe & Bjerkli, 1989). Watts et al. (2023) however, related the late dextral strike-slip kinematics to zeolite-calcite mineralisation on the VF (less distinct on the HSF; D_4 in this study).

The D_4 zeolite and calcite structures, which from field evidence cross-cut the D_1 to D_3 features (Figure 4E & F, and Figure 5G), are not directly dated in this study. However, these veins may have formed after ~150 Ma to ~75 Ma (Table 2, Figure 8B, & Figure 9), owing to cross-cutting relationships (Figure 8B). Similar zeolite-calcite mineralisation has been identified by Tartaglia et al. (2022) and Watts et al. (2023) in other parts of the margin (Hitra and Runde Islands) and on the Fosen Peninsula, where it is associated with the VF (only locally occurring along the HSF). These other studies link the zeolite-calcite structures to a combination of earlier Mesozoic dextral strike-slip to transpressional faulting related to the N-S folds in the Edøyfjorden Basin (D_3 structures), later extensional dip-slip faulting on the HSF post-dating the zeolite-calcite features (Watts et al., 2023), or Late Cretaceous extension in the distal part of the rift margin (Gernigon et al., 2020; Tartaglia et al., 2022).

The NE-SW, NNW-SSE to WNW-ESE D_4 strike trends may therefore preserve evidence of both the earlier Mesozoic (Jurassic) dextral strike-slip movement on the MTFC, associated with the NNW-SSE to WNW-ESE trends and the later Cretaceous to Late Cretaceous extension corresponding to the most frequent orientation trend NE-SW.

Representing the last Cretaceous-Palaeocene deformation episode, the D_5 quartz-calcite veins (Figure 4F, and Figure 5H & I) are similar to calcite veins analysed for U-Pb ages in SW Norway and the WGR (Hestnes et al., 2023). Different veins oriented NE-SW returned ages of ~90 Ma to ~80 Ma, associated with Cretaceous reactivation of the MTFC; ~NW-SE (and NE-SW) veins forming ~70 Ma to 60 Ma, associated with regional uplift owing to doming of the proto-Icelandic plume; and NE-SW veins forming <50 Ma, associated with different Cenozoic extensional process (lithospheric flexure, uplift from far-field tectonic stresses) (Hestnes et al., 2023).

Regionally, the lineament trends associated with both D_4 and D_5 crosscut all the other lineaments (Figure 2B.IV & VI) indicating they are indeed late features. Similar subparallel lineaments are present in isolated parts of Smøla, and to the SE of the HSF in the WGR (Figure 11). Subparallel to the NW-SE D_4 and D_5 lineaments, there are NW-SE SW/NE-dipping normal

https://doi.org/10.5194/egusphere-2023-2504
Preprint. Discussion started: 8 November 2023

faults offsetting the Mesozoic sediments within the Edøyfjorden Basin, which are orthogonal to the HSF (Bøe & Bjerkli, 1989). Overall, the geometries of these faults, lineament, and vein orientations suggest ~E-W to NE-SW crustal extension on average.

Based on geometry and timing, the D_4 and D_5 structures potentially relate to both the Cretaceous reactivation of the MTFC and the Cretaceous-Palaeocene rifting preceding the break-up of Greenland and Norway (Faleide et al., 2008). Importantly, the D_4 and D_5 features are subparallel to extensional structures offshore, particularly to the bounding Klakk Fault Complex on the western side of the Frøya High, the Halten Terrace, as well as the HD to the NW of Hitra and Frøya, suggesting a temporal and geometric association.

5.2 Application to and implications for the Frøya High offshore domain

Frøya High, being analogous to Smøla, is bound to the west by the Klakk Fault Complex, a major west-dipping extensional fault zone, with intrabasement structures located in the footwall of this structure (Muñoz-Barrera et al., 2020). The Frøya High experienced polyphase deformation related to stretching and thinning of the margin during the mid-Carboniferous, Permian-Triassic, and rifting basin development during the Late Jurassic-Early Cretaceous, and eventual break-up during the Late Cretaceous-Palaeocene rifting (Faleide et al., 2008, 2015; Peron-Pinvidic and Osmundsen, 2018). Therefore, the integrated multi-technique approach, and the results of our study on Smøla, which has unravelled a complex polyphase tectonic history, could well be applied to an offshore basement volume such as Frøya High.

The crucial toolset in this study has been four diamond drill holes (Figure 3) in addition to regional datasets including the airborne magnetic data (Figure 2). Numerous drill holes have been completed along the mid-Norway margin (e.g., Slagstad et al., 2008; Bunkholt et al., 2022), with the drill holes over the Frøya High summarised in *Table 5*. The drill hole material from these holes involves only rock cuttings or rock plugs (Muñoz-Barrera et al., 2020). This, along with the lack of drill hole orientation and spatial data available, further highlights how the results from this study on Smøla can assist in constraining basement highs offshore.

Similarly, margin-wide geophysical (magnetic, gravity, and 2D, 3D seismic reflection surveys) datasets are also available (Muñoz-Barrera et al., 2020; Skilbrei et al., 2002). Recently, utilising many of these datasets, Muñoz-Barrera et al. (2020) was able to determine seismic-resolution-scale geometric and segmentation characterisation of the Klakk Fault Complex, as well as identifying three major intrabasement structures within the Frøya High. Additionally, Gresseth et al. (2023) made use of 2D and 3D seismic reflection data to produce 3D geometric and evolution constraints of the Klakk Fault Complex. Both these studies, however, involved interpretations within the seismic resolution-scale, with little information regarding the sub-seismic resolution intrabasement structures. Therefore, to achieve a similar resolution as the Smøla tectonic evolution framework, detailed structural logging of the available drill core/rock cuttings and the ability to undertake microstructural analyses is required.

https://doi.org/10.5194/egusphere-2023-2504
Preprint. Discussion started: 8 November 2023

Table 5. Drill holes over Frøya High with details provided by Slagstad et al. (2008)**, and U-Pb ages of zircon in basement rocks (*) by** Slagstad et al. (2011)**.**

Drill ID	End of hole depth (m)	Top of basement (m)	Geology	Area	U-Pb ages*
6407/10-3	2972.1	2959.0	Granite	Frøya High	436.6 ± 4.4 Ma
6306/10-1	3158.5	2989.0	Diorite	Møre Basin/ Frøya High	446.9 ± 4.1 Ma
6305/12-2	3158.3	3145.0	Brecciated siltstone	Møre Basin	n/a

Fractured and weathered basement is a critical research area in terms of characterising basement-hosted oil and gas reservoirs or fluid pathways (Trice, 2014; Trice et al., 2022). Although out of the scope of this study, the petrophysical attributes of the different deformation features which are related to the D_1 to D_5 deformation episodes may have significant effects on fluid migration or storage along and within relevant deformation features. As these features exhibit cross-cutting relationships and different orientation trends, structural permeability anisotropy is clearly present in the Smøla basement volume. Therefore, producing high resolution structural characterisations aided by the absolute time dimension, may be crucial in understanding basement-hosted plays offshore.

6 Conclusions

The toolbox approach proposed by this study, integrating various methodologies and data types including multiscalar geophysical, drill core, outcrop, 3D modelling, microstructural datasets, and geochronological results, results in the following key conclusions:

1) From regional to microscale evidence, at least five distinct tectonic events have been recognised as having affected Smøla since the Devonian (Figure 11):
   I. The earliest syn- to post-Devonian ENE-WSW, WNW-ESE to NW-SE striking epidote-prehnite brittle structures are associated with brittle sinistral transtension along the MTFC, owing to post-Caledonian extension of the margin.
   II. Subsequently, Carboniferous to Late Triassic NE-SW or NW-SE striking sericite-chlorite-calcite shear features, are linked to at least two brittle-ductile phases, associated with sinistral and dextral strike-slip faulting along the MTFC. NE-SW crustal stretching and rifting of the margin, Late Palaeozoic basins formation relate to the sinistral faulting, and possible late margin-wide slab-push forces acting on the MTFC resulted in the dextral faulting.
   III. Next, NE-SW, NNE-SSW to N-S striking chloritic-hematite breccias and gouges, which developed owing to Mesozoic crustal extension, basin development, with hematite being introduced from migrating hydrothermal fluids along basin flanking structures.

https://doi.org/10.5194/egusphere-2023-2504
Preprint. Discussion started: 8 November 2023

IV. Later, NE-SW to NNW-SSE and WNW-ESE striking hematite-zeolite-calcite structures, frequently associated with reactivated pre-existing features, is related to both late Mesozoic dextral strike-slip movement on the MTFC, and ~E-W crustal extension owing to regional stretching and rifting.

V. The final, possible Cretaceous to Paleogene NW-SE, WNW-ESE and NNE-SSW striking quartz-calcite veins which cross-cutting all previous deformation features. These mostly tensile veins may have formed from continued ~E-W/ NE-SW crustal extension of the margin.

2) The 3D modelling of the structures demonstrates the complex geometric characteristics of basement deformation, with the features all forming intricate cross-cutting and intersecting structural arrays. Structures corresponding to different deformation episodes require modelling at different scales, with the structures possessing various aperture widths, down-dip and strike extents by deformation episode. Overall, the D_2 structures possess the greatest size/strike extents, and the D_1 features the most localised. Additionally, the modelling confirms that some of the features can be linked to adjacent major structures, such as the D_2 structures being inclined splays from the nearby major E-W structures.

3) Dating of fault gouge material by K-Ar geochronology yielded ages from 314.9 ± 5.4 Ma to 74.7 ± 1.7 Ma, associated with structures related to different deformation episodes. The results associated with the D_2 structures involve K-Ar age results of between ~300 Ma and ~200 Ma, with the D_3 structures associated with younger ages of ~200 Ma to ~100 Ma, and associated D_4 structures providing ages of ~150 Ma to ~75 Ma.

This study therefore offers a promising approach to unravelling the tectonic evolution and structural characterisation of basement blocks that have accommodated long and complex geological histories. The toolbox approach used here also has application in the offshore domain and may help to further understand offshore basement structures such as the Frøya High, and fracture-hosted unconventional hydrocarbon reservoirs related to these basement features.

Data availability

Relevant data analysed including lineament shapefiles, field, drill structural, and XRD and K-Ar geochronology data are available at https://data.mendeley.com/datasets/2nmr2cz9yy/1 (last access 27 October 2023).

Supplement

The supplement related to this article is available online at: https://data.mendeley.com/datasets/2nmr2cz9yy/1

https://doi.org/10.5194/egusphere-2023-2504
Preprint. Discussion started: 8 November 2023

Author contributions

MH undertook conceptualisation, data collection, sample collection, data curation, formal analysis, investigation, validation, writing-original draft and review and editing, and figure preparation. GVK did conceptualisation, data collection, sample collection, writing-final draft and review and editing. JK performed funding acquisition, conceptualisation, contribution-final draft, and review. RvdL undertook sample collection, K-Ar geochronology laboratory analyses, writing-final draft and review and editing. JS did XRD, and K-Ar geochronology laboratory analyses, writing-final draft and review and editing. ØN performed data collection, writing-final draft and review and editing. MB managed the drilling on Smøla Island. AN, undertook data collection, writing-final draft and review and editing. GV undertook funding acquisition, project administration, conceptualisation, data collection, sample collection, PhD project supervision, writing-final draft and review and editing.

Financial support

This research has been supported by the ongoing BASE 3 project ("BASE – Basement fracturing and weathering on - and offshore Norway"); and the Research Council of Norway (Norges Forskningsråd), grant no. 319849. BASE is a joint research project launched and steered by the Geological Survey of Norway (NGU), with the industry partners Equinor ASA, Lundin Norway AS, AkerBP ASA, Spirit Energy Norway AS, and Wintershall-Dea Norway AS, and the Norges Forskningsråd (NFR).

Acknowledgements

We thank all the BASE colleagues for the continuous discussion and constructive inputs. The NGU petrography laboratory is thanked for the assistance in the preparation of the thin sections. Also, all the colleagues at the University of Bologna are specially thanked for their continual support and encouragement.

References

Belaidi, A., Bonter, D.A., Slightam, C., and Trice, R.C., 2018, The Lancaster Field: Progress in opening the UK's fractured basement play: Petroleum Geology Conference Proceedings, v. 8, p. 385–398, doi:10.1144/PGC8.20.

Blenkinsop, T., Doyle, M., and Nugus, M., 2015, A unified approach to measuring structures in orientated drill core, in Geological Society Special Publication, Geological Society of London, v. 421, p. 99–108, doi:10.1144/SP421.1.

Bøe, R., Atakan, K., and Sturt, B.A., 1989, The style of deformation in on Hitra and Smøla. Central: Norges Geologiske Undersøkelse Bulletin, v. 414, p. 1–19.

https://doi.org/10.5194/egusphere-2023-2504
Preprint. Discussion started: 8 November 2023

Bøe, R., and Bjerkli, K., 1989, Mesozoic sedimentary rocks in Edøyfjorden and Beitstadfjorden, Central Norway: Implications for the structural history of the Møre-Trøndelag Fault Zone: Marine Geology, v. 87, p. 287–299, doi:https://doi.org/10.1016/0025-3227(89)90066-2.

Bonter, D.A., and Trice, R., 2019, An integrated approach for fractured basement characterization: The lancaster field, a case study in the UK: Petroleum Geoscience, v. 25, p. 400–414, doi:10.1144/petgeo2018-152.

Brunton, D.L., and Bockelie, J.F., 1979, The Ordovician Sedimentary Sequence on Smøla, West Central Norway: Norges Geologiske Undersøkelse Bulletin, v. 348, p. 21–31.

Bunkholt, H.S.S., Oftedal, B.T., Hansen, J.A., Løseth, H., and Kløvjan, O.S., 2022, Trøndelag Platform and Halten–Dønna Terraces Composite Tectono-Sedimentary Element, Norwegian Rifted Margin, Norwegian Sea: Geological Society, London, Memoirs, v. 57, doi:10.1144/m57-2017-13.

Ceccato, A., Viola, G., Tartaglia, G., and Antonellini, M., 2021, In–situ quantification of mechanical and permeability properties on outcrop analogues of offshore fractured and weathered crystalline basement: Examples from the Rolvsnes granodiorite, Bømlo, Norway: Marine and Petroleum Geology, v. 124, doi:10.1016/j.marpetgeo.2020.104859.

Corfu, F., Andersen, T.B., and Gasser, D., 2014, The Scandinavian Caledonides: Main features, conceptual advances and critical questions: Geological Society Special Publication, v. 390, p. 9–43, doi:10.1144/SP390.25.

Davids, C., Wemmer, K., Zwingmann, H., Kohlmann, F., Jacobs, J., and Bergh, S.G., 2013, K-Ar illite and apatite fission track constraints on brittle faulting and the evolution of the northern Norwegian passive margin: Tectonophysics, v. 608, p. 196–211, doi:10.1016/j.tecto.2013.09.035.

Drake, H., Tullborg, E.L., and Page, L., 2009, Distinguished multiple events of fracture mineralisation related to far-field orogenic effects in Paleoproterozoic crystalline rocks, Simpevarp area, SE Sweden: Lithos, v. 110, p. 37–49, doi:10.1016/J.LITHOS.2008.12.003.

Faleide, J.I., Bjørlykke, K., and Gabrielsen, R.H., 2015, Geology of the Norwegian Continental Shelf, in Bjørlykke, K. ed., Petroleum Geoscience: From Sedimentary Environments to Rock Physics, Berlin, Heidelberg, Springer Berlin Heidelberg, p. 603–637, doi:10.1007/978-3-642-34132-8_25.

Faleide, J.I., Tsikalas, F., Breivik, A.J., Mjelde, R., Ritzmann, O., Engen, Ø., Wilson, J., and Eldholm, O., 2008, Structure and evolution of the continental margin off Norway and the Barents Sea: International Union of Geological Sciences, v. 31, p. 82–91, doi:10.18814/epiiugs/2008/v31i1/012.

Fediuk, F., and Siedlecki, S., 1977, Smøla. Description of the geological map (AMS-M 711) 1321 I - 1:50 000: Universitetsforlaget.

Fossen, H., 2010, Extensional tectonics in the North Atlantic Caledonides: A regional view: Geological Society Special Publication, v. 335, doi:10.1144/SP335.31.

Fossen, H., 1992, The role of extensional tectonics in the Caledonides of South Norway: Journal of Structural Geology, v. 14, p. 1033–1046.

https://doi.org/10.5194/egusphere-2023-2504
Preprint. Discussion started: 8 November 2023

Fossen, H., Khani, H.F., Faleide, J.I., Ksienzyk, A.K., and Dunlap, W.J., 2017, Post-Caledonian extension in the West Norway-northern North Sea region: The role of structural inheritance, in Geological Society Special Publication, Geological Society of London, v. 439, p. 465–486, doi:10.1144/SP439.6.

Fossen, H., Ksienzyk, A.K., Rotevatn, A., Bauck, M.S., and Wemmer, K., 2021, From widespread faulting to localised rifting: Evidence from K-Ar fault gouge dates from the Norwegian North Sea rift shoulder: Basin Research, v. 33, p. 1934–1953, doi:10.1111/bre.12541.

Gautneb, H., 1988, Structure, age and formation of dykes on the island of Smøla, Central Norway: Norsk geologisk tidsskrift, v. 68, p. 275–288.

Gautneb, Ha., and Roberts, D., 1989, Geology and petrochemistry of the Smøla-Hitra batholith, Central Norway: Norges Geologiske Undersøkelse Bulletin, v. 416, p. 1–24.

Gee, D.G., Fossen, H., Henriksen, N., and Higgins, A.K., 2008, From the Early Paleozoic Platforms of Baltica and Laurentia to the Caledonide Orogen of Scandinavia and Greenland: International Union of Geological Sciences, v. 31, p. 44–51, doi:10.18814/epiiugs/2008/v31i1/007.

Geological Survey of Norway, 2021, Bedrock map of Norway 1:1 350 000.:

Gernigon, L., Franke, D., Geoffroy, L., Schiffer, C., Foulger, G.R., and Stoker, M., 2020, Crustal fragmentation, magmatism, and the diachronous opening of the Norwegian-Greenland Sea: Earth-Science Reviews, v. 206, p. 102839, doi:10.1016/J.EARSCIREV.2019.04.011.

Gillespie, P.A., Holdsworth, R.E., Long, D., Williams, A., and Gutmanis, J.C., 2020, Introduction: geology of fractured reservoirs: Journal of the Geological Society, v. 178, p. jgs2020-197, doi:10.1144/jgs2020-197.

Gresseth, J.L.S., Osmundsen, P.T., and Péron-Pinvidic, G., 2023, 3D Evolution of Detachment Fault Systems in Necking Domains: Insights From the Klakk Fault Complex and the Frøya High, Mid-Norwegian Rifted Margin: Tectonics, v. 42, p. e2022TC007600, doi:https://doi.org/10.1029/2022TC007600.

Grønlie, A., and Roberts, D., 1989, Resurgent strike-slip duplex development along the Hitra-Snåsa and Verran Faults, Møre-trøndelag fault zone, Central Norway: Journal of Structural Geology, v. 11, p. 295–305, doi:10.1016/0191-8141(89)90069-2.

Hartz, E.H., B. Martinsen, B., Øverli, P.E., Lie, H., Ditcha, E.M., Schmid, D.W., and Medvedev, S., 2013, Newly Discovered Giant Oil Fields of North Sea - The Role of Fractured Basement Highs, in European Association of Geoscientists & Engineers, p. cp-365-00017, doi:10.3997/2214-4609.20131805.

Hestnes, Å., Drost, K., Sømme, T.O., Gasser, D., Scheiber, T., Linge, H., Chew, D., and Jacobs, J., 2023, Constraining the tectonic evolution of rifted continental margins by U-Pb calcite dating:, doi:10.1038/s41598-023-34649-z.

Holcombe, R., 2013, Oriented Drillcore: Measurement, Conversion and QA/QC Procedures for Structural and Exploration Geologists: http://www.holcombe coughlinoliver.com/downloads/,.

Holdsworth, R.E., McCaffrey, K.J.W., Dempsey, E., Roberts, N.M.W., Hardman, K., Morton, A., Feely, M., Hunt, J., Conway, A., and Robertson, A., 2019, Natural fracture propping and earthquake-induced oil migration in fractured basement reservoirs: Geology, v. 47, p. 700–704, doi:10.1130/G46280.1.

https://doi.org/10.5194/egusphere-2023-2504
Preprint. Discussion started: 8 November 2023

Indrevær, K., Stunitz, H., and Bergh, S.G., 2014, On Palaeozoic–Mesozoic brittle normal faults along the SW Barents Sea margin: Fault processes and implications for basement permeability and margin evolution: Journal of the Geological Society, v. 171, p. 831–846, doi:10.1144/jgs2014-018.

Kendrick, M.A., Eide, A., Roberts, D., and Osmundsen, P.T., 2004, The Middle to Late Devonian Høybakken detachment, central Norway: 40Ar–39Ar evidence for prolonged late/post-Scandian extension and uplift: Geological Magazine, v. 141, p. 329–344, doi:10.1017/S0016756803008811.

Ksienzyk, A.K., Wemmer, K., Jacobs, J., Fossen, H., Schomberg, A.C., Süssenberger, A., Lünsdorf, N.K., and Bastesen, E., 2016, Post-Caledonian brittle deformation in the Bergen area,West Norway: results from K–Ar illite fault gouge dating: Norwegian Journal of Geology, v. 96, p. 275–299, doi:10.17850/njg96-3-06.

Mosar, J., Eide, E.A., Osmundsen, P.T., Sommaruga, A., and Torsvik, T.H., 2002, Greenland – Norway separation: A geodynamic model for the North Atlantic: Norwegian Journal of Geology, v. 82, p. 282–299.

Muñoz-Barrera, J.M., Rotevatn, A., Gawthorpe, R.L., Henstra, G.A., and Kristensen, T.B., 2020, The role of structural inheritance in the development of high-displacement crustal faults in the necking domain of rifted margins: The Klakk Fault Complex, Frøya High, offshore mid-Norway: Journal of Structural Geology, v. 140, doi:10.1016/j.jsg.2020.104163.

Nasuti, A., Olesen, O., Baranwal, O., and Dumais, M., 2015, Compilation of aeromagnetic data, in Olesen, O. et al. eds., Coop Phase 2 - Crustal Onshore-Offshore Project. NGU confidential Report , Norges Geologiske Undersøkelse, v. 063, p. 11–24.

Olsen, E., Gabrielsen, R.H., Braathen, A., and Redfield, T.F., 2007, Fault systems marginal to the Møre-Trøndelag Fault Complex, Osen-Vikna area, Central Norway: Norwegian Journal of Geology, v. 87, p. 59–73.

Osmundsen, P.T., Eide, E.A., Haabesland, N.E., Roberts, D., Andersen, T.B., Kendrick, M., Bingen, B., Braathen, A., and Redfield, T.F., 2006, Kinematics of the Høybakken detachment zone and the Møre–Trøndelag Fault Complex, central Norway: Journal of the Geological Society, v. 163, p. 303–318, doi:10.1144/0016-764904-129.

Pascal, C., and Gabrielsen, R.H., 2001, Numerical modeling of Cenozoic stress patterns in the mid-Norwegian margin and the northern North Sea: Tectonics, v. 20, p. 585–599, doi:https://doi.org/10.1029/2001TC900007.

Peron-Pinvidic, G., Manatschal, G., and Osmundsen, P.T., 2013, Structural comparison of archetypal Atlantic rifted margins: A review of observations and concepts: Marine and Petroleum Geology, v. 43, p. 21–47, doi:10.1016/J.MARPETGEO.2013.02.002.

Peron-Pinvidic, G., and Osmundsen, P.T., 2020, From orogeny to rifting: insights from the Norwegian 'reactivation phase': Scientific Reports, v. 10, doi:10.1038/s41598-020-71893-z.

Peron-Pinvidic, G., and Osmundsen, P.T., 2018, The Mid Norwegian - NE Greenland conjugate margins: Rifting evolution, margin segmentation, and breakup: Marine and Petroleum Geology, v. 98, p. 162–184, doi:10.1016/j.marpetgeo.2018.08.011.

Redfield, T.F., Torsvik, T.H., Andriessen, P.A.M., and Gabrielsen, R.H., 2004, Mesozoic and Cenozoic tectonics of the Møre Trøndelag Fault Complex, central Norway: constraints from new apatite fission track data: Physics and Chemistry of the Earth, Parts A/B/C, v. 29, p. 673–682, doi:https://doi.org/10.1016/j.pce.2004.03.005.

https://doi.org/10.5194/egusphere-2023-2504
Preprint. Discussion started: 8 November 2023

Riber, L., Dypvik, H., and Sørlie, R., 2015, Altered basement rocks on the Utsira High and its surroundings, Norwegian North Sea: Norwegian Journal of Geology, v. 95, p. 57–89.

Roberts, D., 1980, Petrochemistry and palaeogeographic setting of the Ordovician volcanic rocks of Smøla, central Norway: Norges Geologiske Undersøkelse Bulletin, v. 359, p. 43–60.

Roberts, D., and Gee, D.G., 1985, An introduction to the structure of the Scandinavian Caledonides., in The Caledonide orogen–Scandinavia and related areas, v. Part 1, p. 55–68.

Rønning, J.S., and Elvebakk, H., 2005, Onshore-Offshore Resistivity studies. Basement resistivity at the Frøya High.:

Scheiber, T., and Viola, G., 2018, Complex Bedrock Fracture Patterns: A Multipronged Approach to Resolve Their Evolution in Space and Time: Tectonics, v. 37, p. 1030–1062, doi:10.1002/2017TC004763.

Scheiber, T., Viola, G., Wilkinson, C.M., Ganerød, M., Skår, Ø., and Gasser, D., 2016, Direct 40Ar/39Ar dating of Late Ordovician and Silurian brittle faulting in the southwestern Norwegian Caledonides: Terra Nova, v. 28, p. 374–382, doi:10.1111/ter.12230.

Seequent, T.B.S.C., 2022, Leapfrog Works:

Seranne, M., 1992, Late Paleozoic kinematics of the Møre-Trøndelag Fault Zone and adjacent areas, central Norway: Norsk Geologisk Tidsskrift, v. 72, p. 141–158.

Sherlock, S.C., Watts, L.M., Holdsworth, R.E., and Roberts, D., 2004, Dating fault reactivation by Ar/Ar laserprobe: an alternative view of apparently cogenetic mylonite–pseudotachylite assemblages: Journal of the Geological Society, v. 161, p. 335–338, doi:10.1144/0016-764903-160.

Skilbrei, J.R., Olesen, O., Osmundsen, P.T., Kihle, O., Aaro, S., and Fjellanger, E., 2002, A study of basement structures and onshore-offshore correlations in Central Norway.: Norwegian Journal of Geology, v. 82, p. 263–279.

Slagstad, T., Davidsen, B., and Stephen Daly, J., 2011, Age and composition of crystalline basement rocks on the norwegian continental margin: Offshore extension and continuity of the Caledonian-Appalachian orogenic belt: Journal of the Geological Society, v. 168, p. 1167–1185, doi:10.1144/0016-76492010-136.

Slagstad, T., and Kirkland, C.L., 2018, Timing of collision initiation and location of the Scandian orogenic suture in the Scandinavian Caledonides: Terra Nova, v. 30, p. 179–188, doi:10.1111/ter.12324.

Slagstad, T., Ramstad, R.K., Davidsen, B., and Barrére, C., 2008, Petrophysical and thermal properties of pre-Devonian basement rocks on the Norwegian continental margin:

Stober, I., and Bucher, K., 2007, Hydraulic properties of the crystalline basement: Hydrogeology Journal, v. 15, p. 213–224, doi:10.1007/s10040-006-0094-4.

Tanner, D.C., Buness, H., Igel, J., Günther, T., Gabriel, G., Skiba, P., Plenefisch, T., Gestermann, N., and Walter, T.R., 2020, Fault detection: Understanding Faults: Detecting, Dating, and Modeling, p. 81–146, doi:10.1016/B978-0-12-815985-9.00003-5.

Tartaglia, G., Ceccato, A., Scheiber, T., van der Lelij, R., Schönenberger, J., and Viola, G., 2022, Time-constrained multiphase brittle tectonic evolution of the onshore mid-Norwegian passive margin: GSA Bulletin, doi:10.1130/b36312.1.

https://doi.org/10.5194/egusphere-2023-2504
Preprint. Discussion started: 8 November 2023

Trice, R., 2014, Basement exploration, West of Shetlands: Progress in opening a new play on the UKCS: Geological Society Special Publication, v. 397, p. 81–105, doi:10.1144/SP397.3.

Trice, R., Hiorth, C., and Holdsworth, R., 2022, Fractured basement play development on the UK and Norwegian rifted margins:

Tsikalas, F., Faleide, J.I., Eldholm, O., and Blaich, O.A., 2012, The NE Atlantic conjugate margins: Regional Geology and Tectonics: Phanerozoic Passive Margins, Cratonic Basins and Global Tectonic Maps, p. 140–201, doi:10.1016/B978-0-444-56357-6.00004-4.

Tucker, R.D., Robinson, P., Solli, A., Gee, D.G., Thorsnes, T., Krogh, T.E., Nordgulen, Ø., and Bickford, M.E., 2004, Thrusting and Extension in the Scandian Hinterland, Norway: New U-Pb Ages and Tectonostratigraphic Evidence: American Journal of Science, v. 304, p. 477–532.

Viola, G., Scheiber, T., Fredin, O., Zwingmann, H., Margreth, A., and Knies, J., 2016, Deconvoluting complex structural histories archived in brittle fault zones: Nature Communications, v. 7, doi:10.1038/ncomms13448.

Viola, G., Torgersen, E., Mazzarini, F., Musumeci, G., van der Lelij, R., Schönenberger, J., and Garofalo, P.S., 2018, New Constraints on the Evolution of the Inner Northern Apennines by K-Ar Dating of Late Miocene-Early Pliocene Compression on the Island of Elba, Italy: Tectonics, v. 37, p. 3229–3243, doi:https://doi.org/10.1029/2018TC005182.

Viola, G., Venvik Ganerød, G., and Wahlgren, C.-H., 2009, Unraveling 1.5 Ga of brittle deformation history in the Laxemar-Simpevarp area, southeast Sweden: A contribution to the Swedish site investigation study for the disposal of highly radioactive nuclear waste:, doi:10.1029/2009TC002461.

Watts, L.M., 2001, The walls boundary fault zone and the Møre Trøndelag fault complex: a case study of two reactivated fault zones. [PhD thesis]: Durham University, 0–550 p.

Watts, L.M., Holdsworth, R.E., Roberts, D., Sleight, J.M., and Walker, R.J., 2023, Structural evolution of the reactivated Møre-Trøndelag Fault Complex, Fosen Peninsula, Norway: Journal of the Geological Society, doi:10.1144/jgs2022-139.

White, N. C. (2014). Geological Interpretation of Aeromagnetic Data (David J. Isles and Leigh R. Rankin). Economic Geology, 109(5), 1495–1496. https://doi.org/10.2113/econgeo.109.5.1495.

Zastrozhnov, D., Gernigon, L., Gogin, I., Planke, S., Abdelmalak, M.M., Polteau, S., Faleide, J.I., Manton, B., and Myklebust, R., 2020, Regional structure and polyphased Cretaceous-Paleocene rift and basin development of the mid-Norwegian volcanic passive margin: Marine and Petroleum Geology, v. 115, doi:10.1016/j.marpetgeo.2020.104269.